

Nebular abundance gradient in the Cartwheel galaxy using MUSE data

Javier Zaragoza-Cardiel ^{1,2}★, V. Mauricio A. Gómez-González ³, Divakara Mayya ¹
and Gerardo Ramos-Larios ^{4,5}

¹*Instituto Nacional de Astrofísica, Óptica y Electrónica, Luis Enrique Erro 1, Tonantzintla 72840, Puebla, Mexico*

²*Consejo Nacional de Ciencia y Tecnología, Av. Insurgentes Sur 1582, 03940 Mexico City, Mexico*

³*Institute for Physics and Astronomy, Universität Potsdam, Karl-Liebknecht-Str. 24/25, D-14476 Potsdam, Germany*

⁴*Instituto de Astronomía y Meteorología, CUCEI, Univ. de Guadalajara, Av. Vallarta 2602, Arcos Vallarta, 44130 Guadalajara, Mexico*

⁵*CUCEI, Universidad de Guadalajara, Blvd. Marcelino García Barragán 1421, 44430 Guadalajara, Jalisco, Mexico*

Accepted 2022 May 18. Received 2022 May 13; in original form 2021 December 2

ABSTRACT

We here present the results from a detailed analysis of nebular abundances of commonly observed ions in the collisional ring galaxy Cartwheel using the Very Large Telescope (VLT) Multi-Unit Spectroscopic Explorer (MUSE) data set. The analysis includes 221 H II regions in the star-forming ring, in addition to 40 relatively fainter H α -emitting regions in the spokes, disc, and the inner ring. The ionic abundances of He, N, O, and Fe are obtained using the direct method (DM) for 9, 20, 20, and 17 ring H II regions, respectively, where the S⁺⁺ temperature-sensitive line is detected. For the rest of the regions, including all the nebulae between the inner and the outer ring, we obtained O abundances using the strong-line method (SLM). The ring regions have a median $12 + \log \frac{\text{O}}{\text{H}} = 8.19 \pm 0.15$, $\log \frac{\text{N}}{\text{O}} = -1.57 \pm 0.09$ and $\log \frac{\text{Fe}}{\text{O}} = -2.24 \pm 0.09$ using the DM. Within the range of O abundances seen in the Cartwheel, the N/O and Fe/O values decrease proportionately with increasing O, suggesting local enrichment of O without corresponding enrichment of primary N and Fe. The O abundances of the disc H II regions obtained using the SLM show a well-defined radial gradient. The mean O abundance of the ring H II regions is lower by ~ 0.1 dex as compared to the extrapolation of the radial gradient. The observed trends suggest the preservation of the pre-collisional abundance gradient, displacement of most of the processed elements to the ring, as predicted by the recent simulation by Renaud et al., and post-collisional infall of metal-poor gas in the ring.

Key words: galaxies: star clusters – galaxies: individual – galaxies: abundances.

1 INTRODUCTION

The Cartwheel (a.k.a ESO 350-40 or A0035-324) is considered the archetype of collisional ring galaxies (Appleton & Struck-Marcel 1996; Struck 2010). These type of galaxies are formed as a result of a compact galaxy plunging through a massive gas-rich disc galaxy close to its centre and almost perpendicular to it (Lynds & Toomre 1976) and are characterized by a ring that harbours a chain of star-forming knots (Higdon 1995; Marston & Appleton 1995). In classical models of ring galaxies, the star formation (SF) is triggered by a radially expanding density wave that leaves behind the older generations of stars towards the centre (Marcum, Appleton & Higdon 1992; Appleton & Marston 1997). In a recent hydrodynamical simulation that treats SF at parsec scales, Renaud et al. (2018) find that the wave drags the gas and recently formed stars along with it to the present location of the ring.

The chemical properties of the disc and the star-forming ring in the two scenarios presented above are distinctly different. The products of nucleosynthesis expelled from stars are accumulated in the ring in the scenario presented by Renaud et al. (2018), whereas they stay at the location where the stars formed in the classical scenario

(see e.g. Korchagin, Vorobyov & Mayya 1999). Data on chemical abundances on ring galaxies are scarce and do not cover the spatial extent required to test the two scenarios. The most extensive study was carried out by Bransford et al. (1998), who obtained O and N abundances from long-slit spectroscopic data for 28 H II regions in the star-forming ring of eight northern ring galaxies. Their empirically determined O abundances were uniform over the sample, thus ruling out prompt local enrichment. More recently, Kouroumpatzakis et al. (2021) found a radial abundance gradient in the C-shaped ring galaxy NGC 922, using empirically derived O abundances of eight H II regions. For the Cartwheel, Fosbury & Hawarden (1977) measured an O abundance of $12 + \log(\text{O}/\text{H}) \sim 8.0$ and $\log(\text{N}/\text{O}) = -1.5$, using optical spectra of three of the brightest ring H II regions.

The Cartwheel has been the target of Multi-Unit Spectroscopic Explorer (MUSE) observations at the Very Large Telescope (VLT), that covers the entire optical extent of the galaxy at the seeing-limited spatial resolution of ~ 0.6 arcsec. The spectra span a rest wavelength range from ~ 4610 to ~ 9075 Å, which includes emission lines from different ionic species suitable for the determination of abundances of commonly reported elements covering the entire galaxy. At the distance of the Cartwheel (128 Mpc using the Hubble constant of $71 \text{ km s}^{-1} \text{ Mpc}^{-1}$ and velocity = 9050 km s^{-1}), MUSE spectra are available at physical scales of ~ 370 pc. On the H α image constructed using this data set, we have identified 221 individual

* E-mail: javier.zaragoza@inaoep.mx

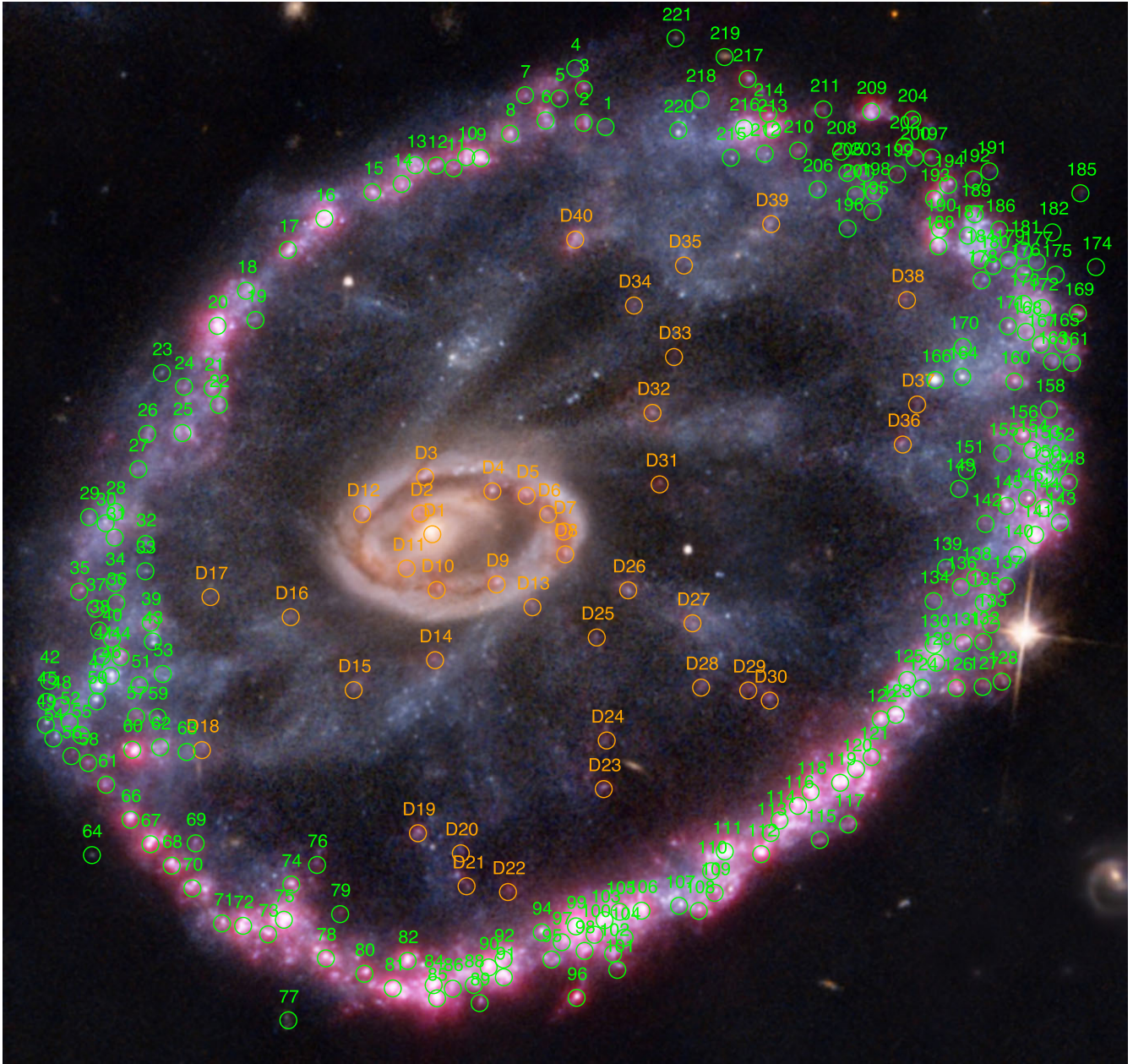


Figure 1. Colour-composite image of the Cartwheel galaxy formed using the *HST*/WFPC2 images (PSF = 0.2 arcsec) in F814W, pseudo-green and F450W as red, green, and blue components, respectively; and the $H\alpha$ image constructed from MUSE data (PSF = 0.6 arcsec) as a fourth reddish component. The HII regions in the outer ring and interior to the outer ring are identified by green and orange circles, respectively. The circles are of 0.6 arcsec radius, which corresponds to 370 pc at the distance of the Cartwheel.

HII regions in the star-forming outer ring and 40 regions in the apparently quiescent inner zones, including around 10 regions in the inner ring. These regions are identified in a colour-composite image formed using this $H\alpha$ image in Fig. 1. This data set offers an excellent opportunity to confront the predictions of the two scenarios of ring formation discussed above.

This article is organized as follows. In Section 2 we describe the data set, extraction of individual spectra and details of measurement of line fluxes. Techniques followed for the determination of abundances are described in Section 3. Detailed discussions based on the reported abundances are presented in the context of the scenarios for the formation of ring galaxies in Section 4. We present our conclusions in Section 5.

2 SPECTROSCOPIC DATA

2.1 VLT/MUSE observations

MUSE is a panoramic integral-field spectrograph at the 8 m VLT of the European Southern Observatory (ESO),¹ operating in the optical wavelength range from 4750 to 9351 Å with a spatial sampling of 0.2 arcsec pixel⁻¹, a spectral sampling of 1.25 Å pixel⁻¹ and a spectral resolution ~ 3 Å (Bacon et al. 2010). The public MUSE data cube covering the entire Cartwheel galaxy was retrieved from the

¹<http://muse-vlt.eu/science/>

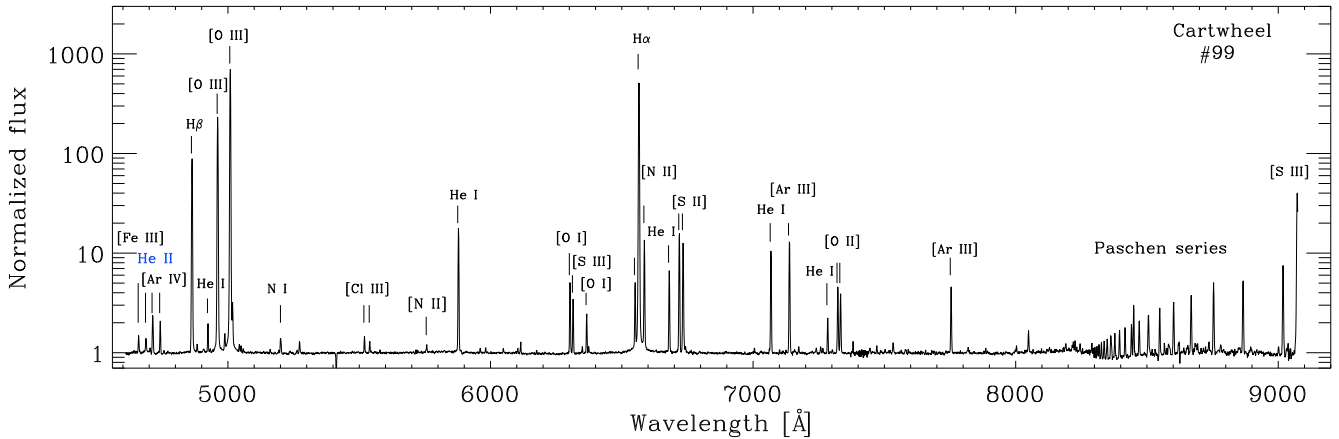


Figure 2. VLT MUSE redshift corrected spectrum of cluster #99 in the Cartwheel. The most common nebular lines are indicated. The spectrum is shown normalized to the best-fitting continuum spectrum.

ESO Science Archive Facility.² The data cube was already flux and wavelength calibrated, and hence, ready for scientific exploitation. The observations were carried out during three runs on 2014 August 24 and 25 (PI: science verification, MUSE) with an effective exposure time of ≈ 4030 s. The observations covered a field of view (FoV) of 2×2 arcmin², which encloses the entire star-forming ring of the Cartwheel, as can be seen in Fig. 1. Milky Way Galactic extinction in the Cartwheel galaxy line of sight is minimal, $A_V = 0.0285$ mag (Schlafly & Finkbeiner 2011), so we do not correct for this effect. As an example, we show in Fig. 2 the MUSE rest-frame spectrum for the brightest H II region in the Cartwheel, designated as region #99 in this study. Prominent nebular lines are identified in the spectrum, that covers the [Fe III] $\lambda 4658$ and [S III] $\lambda 9069$ lines at the two extreme ends.

2.2 MUSE data cube and astrometry

We used the reduced 3D data cube as a starting point in our analysis. The tool QFITSVIEW³ (Ott 2012) was used for the extraction of images at selected wavelengths, as well as spectra of selected regions. A continuum image covering the entire spectral range of MUSE is prepared to facilitate the astrometric calibration of the image. We used the astrometrically calibrated *K*-band image by Barway, Mayya & Robleto-Orús (2020) to transform the MUSE and the *Hubble Space Telescope* (*HST*) images into the International Celestial Reference System (ICRS) as defined by the coordinates of the point sources in the 2MASS catalogue. For this purpose, we identified point sources in the FoV of the MUSE image that are present in the deep *K*-band image and/or the *HST* images. We first astrometrized the *HST* images, which are then used to astrometrize the MUSE images. The astrometric calibration was carried out with the help of IRAF⁴ tasks *cmap* and *wregister*. Sixteen point sources were identified on the MUSE image which resulted in the final absolute astrometric precision of 0.1 arcsec.

2.3 Identifications of nebulae and spectral extraction

As a first step, we generated a continuum-free $H\alpha$ image from the MUSE datacube using the scripts in QFITSVIEW. For achieving this,

we summed fluxes in a 20 Å window centred on $H\alpha$ at the redshifted wavelength of the nucleus of the Cartwheel (sum of pixel numbers between 1605 and 1620 in the wavelength axis) and subtracted a continuum image from it, which is obtained as average of two images 37.5 Å away on either side of the $H\alpha$ line. On this continuum-free $H\alpha$ image (the reddish component in Fig. 1), we visually identified 221 H II regions in and around the outer ring⁵ and 40 regions in the region between the nucleus and the outer ring. Spectra were extracted in apertures of 0.6 arcsec radius around all these visually identified regions.

Higdon (1995) had identified 29 star forming complexes in the outer ring based on an $H\alpha$ image. The MUSE image we have used has a factor of 3 better seeing, allowing us to resolve each complex into several $H\alpha$ -emitting knots. At the resolution of the *HST* image (~ 0.2 arcsec = 125 pc), most of our identified regions are associated with at least one star cluster that is responsible for its ionization. Thus, the selected ring regions are genuine H II regions. On the other hand, the ionized zones selected in the inner disc cannot be associated to identifiable clusters. Furthermore, the extracted spectra of these disc regions showed clear signs for the presence of stellar absorption at $H\beta$, Mg II, and Na I, that are in general broader than the nebular $H\beta$ line. They are likely H II regions ionized by late B-type stars in relatively older fainter clusters, below the detection limit of the *HST* images. We will address elsewhere the nature of the ionization of these sources.

Analysis of nebular abundances requires determination of flux ratios of nebular lines relative to the flux of the $H\beta$ line, which in the inner disc regions is clearly affected by the presence of the underlying absorption feature. We fitted the continuum with population synthesis models using the GIST pipeline (Bittner et al. 2019), which makes use of PPXF (Cappellari 2017) and the MILES library (Vazdekis et al. 2010) to fit the continuum and the absorption lines. The population synthesis was performed over the 4750–7000 Å spectral range, where the MUSE spectral resolution ranges from 3 Å at 4750 Å to 2.5 Å at 7000 Å (Bacon et al. 2017). Therefore, we are able to use the MILES library which has a spectral resolution of 2.5 Å and covers the 3540–7400 Å spectral range (Vazdekis et al. 2010). None of the nebular lines outside of the fitted spectral range are affected by the underlying absorption feature, and hence the flux ratios measured on the observed spectrum are equally good.

²<http://archive.eso.org/cms.html>

³<https://www.mpe.mpg.de/~ott/dpuser/qfitsview.html>

⁴IRAF is distributed by the National Optical Astronomy Observatories, which are operated by the Association of Universities for Research in Astronomy, Inc., under cooperative agreement with the National Science Foundation.

⁵Among the 221 $H\alpha$ -emitting regions, only 212 regions that have $H\beta$ line also in emission are retained in our final analysis.

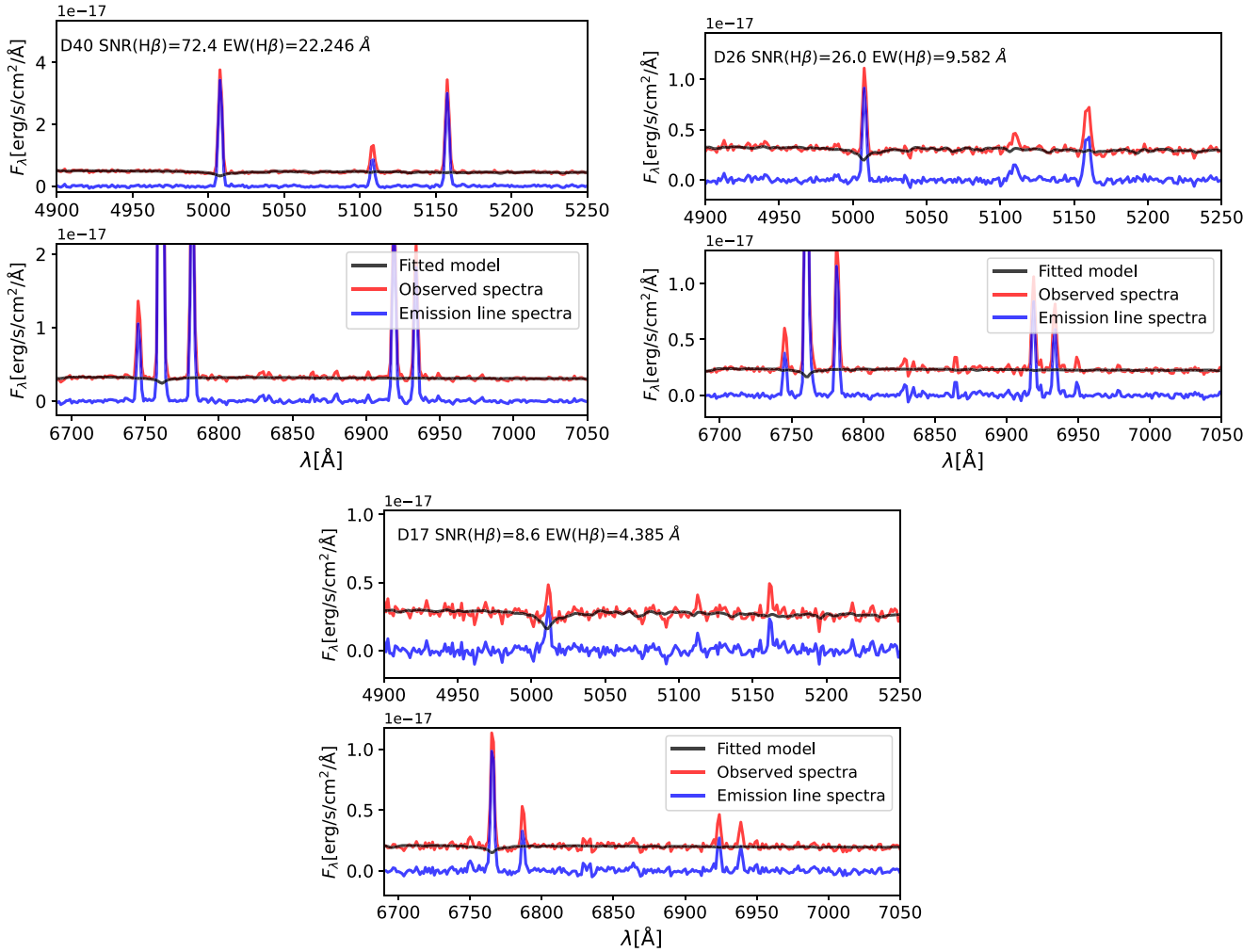


Figure 3. Subtraction of the underlying stellar continuum; spectra of three regions from the inner disc: D40 (top left-hand panel), D26 (top right-hand panel), and D17 (bottom), are shown in two sub-panels each, the top one covering the $H\beta$ line, and the bottom one, the $H\alpha$ line. In each plot, the observed, fitted model and the pure emission line spectra are shown in red, grey and blue, respectively. The three plotted spectra illustrate the effect of the underlying absorption on the measured $H\alpha$ and $H\beta$ lines for relatively high, medium, and low measured $H\beta$ SNRs and $H\beta$ EWs, respectively. The observed, not the rest-frame, spectra are shown in all cases.

We subtracted the fitted continuum to obtain pure nebular spectra, which is the one we used for the abundance analysis in the inner disc regions. We illustrate the fitting and subtraction of the underlying absorption feature in Fig. 3 for three cases: the top left-hand, top right-hand, and bottom panels show spectra for inner disc regions with relatively high, intermediate and low $EW(H\beta)$; these three cases also correspond to high, intermediate, and low $SNR(H\beta)$, respectively. The model spectra (black line) fit very well the observed spectra (blue line) in all three illustrated cases, and hence the model-subtracted spectrum corresponds to a pure nebular spectrum. As expected, the nebular $H\beta$ line is progressively more affected by the underlying absorption as the nebular $EW(H\beta)$ decreases.

Unlike the disc $H\text{II}$ region spectra, the ring $H\text{II}$ region spectra are dominated by nebular lines with no strong-enough absorption feature for a reliable fitting of the continuum with an underlying stellar population. Nevertheless, we took care of the possible presence of weak absorption features at $H\alpha$ and $H\beta$ wavelengths by adding 2 \AA to the EWs of these two lines following the standard procedure advocated by McCall, Rybski & Shields (1985).

2.4 Measurement of line fluxes

The main purpose of the spectral analysis is to measure accurate fluxes of emission lines suitable for nebular abundance measurements. The spectral range of MUSE includes temperature-sensitive lines of $[\text{N II}]$ and $[\text{S III}]$ ions, density-sensitive lines of $[\text{S II}]$, $[\text{Cl III}]$ and $[\text{Ar IV}]$ ions, in addition to lines for determination of abundances of He, O, N, S, Ar, Cl, and Fe. The complete list of lines we measured is available as a supplementary material in a machine readable table (MRT) format. We used the Gaussian profile fitting routine of the *splot* task in IRAF for measuring the fluxes of individual spectral lines. We fitted Gaussian profiles at the redshifted wavelength of each line in the list in an automated way using the cursor command facilities of IRAF. The flux, equivalent width (EW), full-width at half-maximum (FWHM) of each fitted line are stored for analysing the signal-to-noise ratio ($SNR = \text{flux}/\sigma_1$) of each line. The noise in measured flux (σ_1) of each line is calculated using the expression (Tresse et al. 1999):

$$\sigma_1 = \sigma_c D \sqrt{\left(2N_{\text{pix}} + \frac{EW}{D}\right)}, \quad (1)$$

where D is the spectral dispersion in \AA per pixel (1.25 for MUSE), σ_c is the mean standard deviation per pixel of the continuum, which is measured in a line-free part of the continuum adjacent to each line, N_{pix} is the number of pixels covered by the line, which is equated to the FWHM of the fitted Gaussian profile. We imposed the condition that for a line to be considered detected, it should have an $\text{SNR} \geq 4$ and FWHM comparable to that of the $\text{H}\beta$. We used a factor of 2 tolerance in FWHM, which takes into account errors in the FWHM of the fitted Gaussians, especially for the lines at the threshold of detection (flux $\lesssim 1$ per cent of $\text{H}\beta$), such as the temperature sensitive lines of $[\text{N II}] \lambda 5755$ and $[\text{S III}] \lambda 6312$. When a line does not fulfill these criteria, it is assigned a limiting flux of $3 \times \sigma_1$, where we substituted N_{pix} by the FWHM of the $\text{H}\beta$ line.

The $\text{H}\alpha$ -emitting regions detected in the region between the nucleus and the outer ring are, in general, fainter in all lines as compared to their outer ring counterparts. Temperature-sensitive lines are not traced in any of these regions. The diffuse ionized gas (DIG) component can affect the line measurements. Since DIG is related to young and old stars (Belfiore et al. 2022), it is not clear if DIG removal is better for studies like the one presented here. However, we have estimated how much our line estimates can be affected by the DIG. We have defined diffuse regions of the ring with $\text{H}\alpha$ surface brightness $F_{\text{H}\alpha} < 5 \times 10^{-17} \text{erg s}^{-1} \text{cm}^{-2} \text{arcsec}^{-2}$, and extracted the spectrum of these regions. After subtracting the DIG spectrum from the H II regions, we found that the difference in $[\text{N II}]$, $[\text{S II}]$, $[\text{O III}]$ line fluxes are of the order of 0.01 dex for the brightest regions, while as much as 0.08 dex for the faintest regions. Therefore, we decide not remove the DIG since its contribution does not affect the results presented in this work.

The $\text{H}\alpha$ and $\text{H}\beta$ line fluxes for all the regions where the $\text{H}\beta$ line is detected at $\text{SNR} \geq 4$ are used to determine the attenuation from the

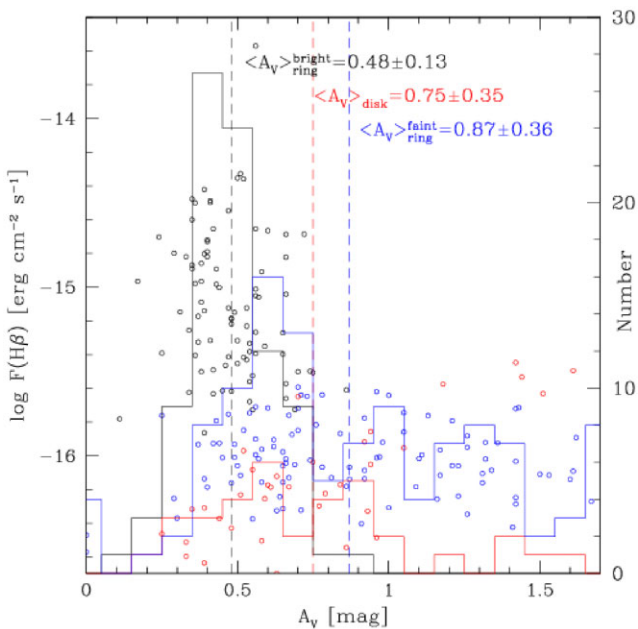


Figure 4. Distribution of A_V for H II regions in the Cartwheel (histogram at the right axis scale). The points show the distribution of the reddening corrected $\text{H}\beta$ flux in each bin of A_V . The values for ring and disc H II regions are shown in blue and red colours, respectively. The average values of A_V for ring and disc samples are shown by the vertical dashed lines of blue and red colours, respectively. The disc H II regions are systematically fainter and reddened than the ring H II regions.

dust in the H II region and along the line of sight. For this purpose, we used the Balmer decrement method for case B recombination of a typical photoionized nebula (Osterbrock & Ferland 2006) and the reddening curve of Cardelli, Clayton & Mathis (1989). The Balmer recombination line ratios are only weakly dependent on T_e and n_e values, and hence we used an intrinsic $\frac{I(\text{H}\alpha)}{I(\text{H}\beta)} = 2.863$ corresponding to $T_e = 10\,000$ K, $n_e = 100 \text{cm}^{-3}$, canonical values for extragalactic H II regions. The choice of these canonical values for the Cartwheel is justified by the directly determined T_e values for the ring H II regions (11 000–15 000 K) and those estimated for the disc regions (~ 8000 – $10\,000$ K) based on the empirical relations of Pilyugin & Grebel (2016) between the O abundance and T_e . The densities in the Cartwheel H II regions are also close to the canonical value used. The A_V values would differ from the calculated values at the most by ± 0.04 mag using the measured/estimated values for each region instead of the canonical values, which is small compared to the range of measured A_V values.

The attenuation-corrected line fluxes normalized to that of the $\text{H}\beta$ line are tabulated in the supplementary MRT table. The error on the line fluxes normalized to that in $\text{H}\beta$ is calculated by propagating the errors on the line of interest and the $\text{H}\beta$ line. The table also contains the A_V values along with the determined errors, the corrected $\text{H}\beta$ flux and the SNR, $\text{H}\alpha$ and $\text{H}\beta$ EWs, as well as the coordinates. For spectra having $\text{SNR}(\text{H}\beta) \geq 40$, we tabulate the $1-\sigma$ upper limits of all lines in the error column.

3 DETERMINATION OF ABUNDANCES

3.1 Determination of ionic and elemental abundances from direct method

Surprisingly, the last published work on the measurement of metallic abundances in the Cartwheel is by Fosbury & Hawarden (1977). Using spectra taken with photographic plates, they reported He, O, N and Ne abundances for two of the brightest regions, referred to as knots A and B, which correspond to our H II region numbers #99 and #119, respectively. The average O abundance they obtained for these two knots is $12 + \log(\text{O}/\text{H}) = 8.0 \pm 0.1$. Using Balmer decrement method for a photoionized nebula, they reported an $E(B - V) = 0.64$, which corresponds to $A_V = 2$ mag for the Galactic extinction curve with $R_V = 3.1$.

The MUSE data set has allowed us to obtain A_V values using H II regions in the ring and the disc. In Fig. 4, we show the distribution of these A_V values, divided into three different groups: bright ring regions, consisting of 88 regions that have at least an SNR of 40 in the $\text{H}\beta$ line; the remaining 103 relatively fainter ring H II regions; and 36 of the 40 disc H II regions that had detectable $\text{H}\beta$ emission.

The mean value for the bright ring sample is 0.48 ± 0.13 mag, with the A_V values for the two regions in common with Fosbury & Hawarden (1977) are 0.56 mag (#99) and 0.35 mag (#119). These values are significantly smaller than the often used value of $A_V = 2$ mag, based on the photographic plate spectra of Fosbury & Hawarden (1977). We believe the non-linearity in the flux calibration of photographic spectra is the reason for the high A_V values reported by Fosbury & Hawarden (1977). In comparison, the fainter ring H II regions and the disc H II regions have mean values of 0.87 ± 0.36 mag and 0.75 ± 0.35 mag, respectively, which are systematically higher as compared to the bright ring regions. We use the measured A_V to deredden all the line fluxes.

The range of A_V values in the Cartwheel are in the range of observed values in extragalactic H II regions (e.g. Sánchez et al.

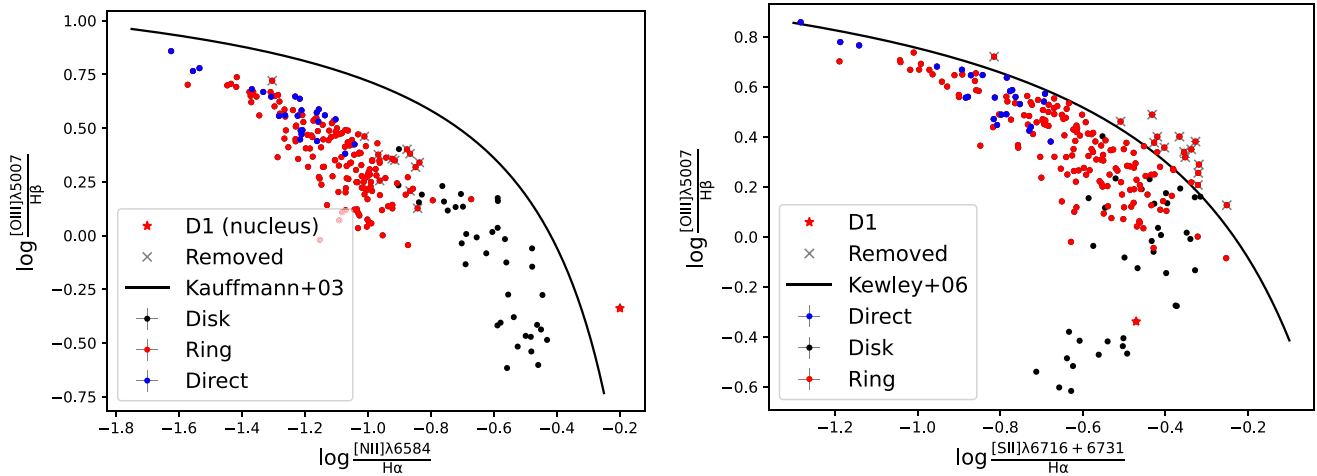


Figure 5. BPT diagrams for the identified regions in Cartwheel; (left-hand panel) $\log \frac{[\text{O III}]\lambda 5007}{\text{H}\beta}$ versus $\log \frac{[\text{N II}]\lambda 6584}{\text{H}\alpha}$ and (right-hand panel) $\log \frac{[\text{O III}]\lambda 5007}{\text{H}\beta}$ versus $\log \frac{[\text{S II}]\lambda 6716+31}{\text{H}\alpha}$. We show the regions from the external ring (red dots), from the inner disc (black dots), the regions where DM abundances were determined (blue dots) and the nuclear region (D1) (red star). Regions photoionized by stars are expected to lie below the curves defined by Kauffmann et al. (2003) (left-hand panel) and Kewley et al. (2006) (right-hand panel). Regions marked by a grey cross may have contribution from shock ionization, and were omitted for the analysis of abundances.

2015; Espinosa-Ponce et al. 2020). However, there is an important difference between the Cartwheel and normal galaxies: brighter regions have systematically higher extinction in normal galaxies, whereas Fig. 4 shows a clear tendency for the brighter H II regions to have lower A_V values. The direct correlation between H β flux and A_V is expected for regions that follow the Kennicutt–Schmidt relation (Barrera-Ballesteros et al. 2020) between the SFR and gas density, as the H β flux is a direct tracer of SFR and A_V is proportional to the gas density. Conversely, the anticorrelation between H β flux and A_V in the Cartwheel indicates a breakdown of Kennicutt–Schmidt relation. Such a breakdown in the Cartwheel has been comprehensively illustrated by Higdon et al. (2015), who obtained total gas densities in the ring regions by combining recent ALMA observations of the molecular gas and the Higdon (1996) HI observations. The most likely reason for the breakdown is the negative feedback, namely destruction of molecular clouds and expulsion of gas, due to winds from massive stars and supernovae (SNe) explosions associated to the recent star formation.

In order to ensure that the emission lines we have measured are due to photoionization associated to star formation, we show in Fig. 5 both the ring and the inner disc regions in the BPT diagrams (Baldwin, Phillips & Terlevich 1981). We show as a black line the curve used to differentiate between star formation and AGNs from Kauffmann et al. (2003), Kewley et al. (2006). In the case of the use of [N II] (Fig. 5, left-hand panel), it is clear that all regions, except one, are well inside the boundary defined for the photoionization by stars. The exception is the region labelled as D1 in Fig. 1 which corresponds to the nucleus of the Cartwheel, and shows LINER-like spectral characteristics. We exclude this region from the analysis in the rest of the paper. In the case of the use of [S II] (Fig. 5, right-hand panel) there are a few regions clearly outside the empirical division for photoionization (Kewley et al. 2006). We do not use those regions that are analysed for the determination of nebular abundances are associated to star formation.

Chemical abundances were calculated using the ‘direct method’ (DM), which requires the measurement of the physical condition of the ionized gas, namely the electron temperature (T_e) and the

electron density (N_e). We used the three zone (high, medium, and low) ionization model of H II regions proposed by Garnett (1992) to determine the ionic abundances. The bluest wavelength of MUSE spectral coverage is ~ 4620 Å at the rest wavelength for Cartwheel, which implies that [O III] $\lambda 4363$, the most commonly used temperature-sensitive line, cannot be used for the determination of the temperature of the high ionization zone ($T_e^{\text{high}} \equiv T_e([\text{O III}])$). However, the spectral range covers the [S III] $\lambda 9069$ line at the red border for majority of the regions which, when combined with [S III] $\lambda 6312$ line, measures the temperature of the medium ionization zone ($T_e^{\text{med}} \equiv T_e([\text{S III}])$). The regions without the [S III] $\lambda 9069$ line fluxes are the ones in the western part of the ring (identification numbers between 22 and 96), which have recessional velocities that shift the line outside the spectral coverage of MUSE. Both the [S III] $\lambda 6312$ and [S III] $\lambda 9069$ lines are detected above an $\text{SNR} > 4$ in 29 of our regions. The spectral range covers all the three [N II] lines for measuring the $T_e([\text{N II}]$), the temperature of the low ionization zone (T_e^{low}). We notice that in the Cartwheel the [N II] $\lambda 5755$ is systematically fainter than the [S III] $\lambda 6312$, allowing the direct determination of T_e^{low} in only 5 of the 24 regions where T_e^{med} has been determined. For the sake of uniformity in the temperature estimations, we preferred to estimate T_e^{low} from T_e^{med} as explained below for all regions, even for the five regions where the [N II] $\lambda 5755$ is detected.

We used the equations obtained by Garnett (1992) using photoionization models to relate the temperatures in the three zones. The T_e for the high ionization zone was obtained for all the regions with T_e^{med} measurements using the relation:

$$T_e^{\text{high}} = 1.2 T_e^{\text{med}} - 2048 \text{ K}, \quad (2)$$

and T_e^{low} using:

$$T_e^{\text{low}} = 0.7 T_e^{\text{high}} + 3000 \text{ K}. \quad (3)$$

Both relations are supported by observational data (e.g. Kennicutt, Bresolin & Garnett 2003; Bresolin et al. 2009; Esteban et al. 2009; Arellano-Córdova & Rodríguez 2020).

The wavelength range covered by the MUSE spectra covers the density-sensitive lines of [S II], [Cl III], and [Ar IV], which originate

Table 1. T_e , N_e , and element abundances determined with the DM for some of the regions in Cartwheel.

ID	$T_e^{\text{low}} (a)$ $\times 10^4$ K	$T_e^{\text{high}} (a)$ $\times 10^4$ K	T_e^{medium} $\times 10^4$ K	$N_e([\text{S II}])$ e^-/cm^3	12+log(O/H)	12+log(Fe/H)	12+log(N/H)	12+log(He/H)
9	1.11 ± 0.04	1.15 ± 0.05	1.05 ± 0.04	50 ± 5	8.38 ± 0.11	5.88 ± 0.15	6.68 ± 0.10	...
10	1.12 ± 0.05	1.17 ± 0.08	1.07 ± 0.06	27.9 ± 3.3	8.35 ± 0.14	5.93 ± 0.17	6.71 ± 0.12	...
12	1.32 ± 0.18	1.45 ± 0.25	1.41 ± 0.21	55 ± 22	8.0 ± 0.4	...	6.5 ± 0.4	...
14	1.20 ± 0.12	1.28 ± 0.18	1.20 ± 0.15	58 ± 13	8.16 ± 0.28	...	6.60 ± 0.24	...
16	1.21 ± 0.05	1.29 ± 0.07	1.22 ± 0.05	55.1 ± 3.5	8.19 ± 0.08	5.87 ± 0.09	6.62 ± 0.07	10.93 ± 0.11
60	1.28 ± 0.05	1.40 ± 0.07	1.34 ± 0.06	109 ± 29	8.07 ± 0.28	5.7 ± 0.4	6.39 ± 0.26	10.89 ± 0.31
98	1.136 ± 0.033	1.19 ± 0.05	1.10 ± 0.04	29.2 ± 2.6	8.34 ± 0.10	5.95 ± 0.12	6.63 ± 0.09	...
99	1.250 ± 0.006	1.357 ± 0.008	1.295 ± 0.007	185 ± 7	8.16 ± 0.04	5.92 ± 0.07	6.44 ± 0.04	10.94 ± 0.04
100	1.16 ± 0.04	1.23 ± 0.05	1.14 ± 0.04	27.9 ± 1.2	8.30 ± 0.06	6.01 ± 0.10	6.61 ± 0.05	10.92 ± 0.07
103	1.17 ± 0.06	1.25 ± 0.09	1.17 ± 0.07	25.6 ± 1.4	8.23 ± 0.09	5.96 ± 0.11	6.61 ± 0.08	...
105	1.20 ± 0.04	1.28 ± 0.06	1.21 ± 0.05	18 ± 6	8.20 ± 0.33	5.87 ± 0.33	6.53 ± 0.31	...
106	1.191 ± 0.030	1.27 ± 0.04	1.195 ± 0.035	24 ± 5	8.21 ± 0.21	5.82 ± 0.25	6.51 ± 0.19	10.90 ± 0.24
108	1.21 ± 0.11	1.30 ± 0.16	1.23 ± 0.13	18.8 ± 2.2	8.11 ± 0.17	5.95 ± 0.19	6.56 ± 0.15	10.89 ± 0.17
111	1.21 ± 0.06	1.30 ± 0.08	1.22 ± 0.07	44 ± 7	8.19 ± 0.17	5.96 ± 0.17	6.51 ± 0.15	...
112	1.53 ± 0.05	1.76 ± 0.08	1.77 ± 0.06	13 ± 6	7.8 ± 0.5	5.5 ± 0.7	6.4 ± 0.4	...
119	1.33 ± 0.07	1.47 ± 0.10	1.43 ± 0.08	1.9 ± 1.3	8.0 ± 0.7	5.8 ± 0.7	6.5 ± 0.7	10.9 ± 0.7
120	1.30 ± 0.10	1.43 ± 0.14	1.38 ± 0.12	12.7 ± 3.4	8.02 ± 0.29	5.83 ± 0.32	6.46 ± 0.27	10.90 ± 0.32
122 ^b	1.55 ± 0.23	1.78 ± 0.33	1.80 ± 0.28	48 ± 14	7.8 ± 0.4	...	6.44 ± 0.33	...
126 ^b	1.8 ± 0.4	2.2 ± 0.5	2.2 ± 0.4	80 ± 40	7.5 ± 0.6	...	6.2 ± 0.6	...
129 ^b	1.53 ± 0.29	1.8 ± 0.4	1.77 ± 0.35	48 ± 11	7.74 ± 0.32	...	6.35 ± 0.29	...
131 ^b	1.55 ± 0.27	1.8 ± 0.4	1.81 ± 0.32	36 ± 18	7.7 ± 0.6	...	6.4 ± 0.5	...
141	1.14 ± 0.06	1.20 ± 0.08	1.11 ± 0.07	57.5 ± 3.2	8.31 ± 0.08	5.99 ± 0.09	6.58 ± 0.08	...
144	1.31 ± 0.09	1.45 ± 0.13	1.40 ± 0.11	72 ± 13	8.00 ± 0.20	5.79 ± 0.20	6.47 ± 0.19	10.92 ± 0.20
156	1.18 ± 0.14	1.25 ± 0.20	1.17 ± 0.16	60 ± 10	8.17 ± 0.23	...	6.69 ± 0.20	...

Note. ^a Not directly estimated from observations, but using equations (2) and (3). ^b Rejected for the DM analysis due to its high determined temperature as compared to that expected from the $T_e - N_{2\text{H}\beta}$ relation (Pilyugin & Grebel 2016).

in low, medium, and high ionization zones, respectively. However, the doublets of [Cl III] and [Ar IV] are faint to obtain reliable measurement of N_e corresponding to the zones in which these ions are found. On the other hand, both the [S II] lines are detected in all the 24 regions, where the temperature-sensitive [S III] line is detected. We hence obtained density from [S II] lines and assumed it to be uniform over the entire H II region for the sake of obtaining abundances from DM.

We used PYNEB (Luridiana, Morisset & Shaw 2015) to determine simultaneously the T_e ([S III]) and N_e ([S II]) using [S III] λ 6312/ λ 9069 and [S II] λ 6717/ λ 6731, respectively, for the 24 regions where both the [S III] λ 6312 and [S III] λ 9069 lines have been detected. The relative flux ratio uncertainties are propagated as the relative uncertainties of T_e and N_e .

Ionic abundances are calculated using PYNEB, where we use as inputs the T_e corresponding to each ionization zone, the N_e estimated previously, as well as the following lines (when detected) for each ion: Fe²⁺ λ 44658, 4881, 4986, 5270; O⁰ λ 6300; O⁺ λ 7320, 7330; O²⁺ λ 44959, 5007; N⁺ λ 46549, 6583; He⁺ λ 44922, 5876, 6678, 7065, 7281; and He⁺⁺ λ 4686. The relative uncertainty of the ionic abundance for each line is determined from the quadratic sum of the relative T_e , N_e , and flux ratio uncertainties. The ionic abundances are obtained by an error weighted average of the ionic abundance for each line.

Finally, we determined the abundance for each element. For O and He we used the direct sum of their ionic abundances in their three states: $N(\text{O}) = N(\text{O}^0) + N(\text{O}^+) + N(\text{O}^{2+})$ and $N(\text{He}) = N(\text{He}^+) + N(\text{He}^{++})$. The equation for He abundance assumes that there is no neutral He in the H ionized volume, which is valid within 2 per cent for high ionization regions that show the He II λ 4686 line (Izotov, Stasińska & Guseva 2013). The He II λ 4686 line is detected in all the 20 regions that are used for abundance measurement from

DM (see Mayya et al. submitted to MNRAS). We report here the He abundance only for the regions where the SNR of the He II λ 4686 is larger than 4, which is fulfilled for nine regions. The presence of He⁺ ion implies that some fraction of O could be in O³⁺ state. We used the ionization correction factor which considers the O³⁺ abundance for the high excited H II regions from Izotov et al. (2006), although the change in the total O abundance because of this correction is as small as 0.7 per cent. For the Fe and N abundances we used the O⁺, O²⁺, with the corresponding element ionic abundances and the intermediate metallicity ($7.6 \leq 12 + \log \frac{\text{O}}{\text{H}} \leq 8.2$) ionization correction factors from Izotov et al. (2006). We present the T_e , N_e , and element abundances used in this work in Table 1.

3.2 Determination of elemental abundances from strong-line method (SLM)

The abundances estimated using the DM are viable just for 24 regions in the external ring. In order to estimate the O abundances over the whole system, we used empirical strong line calibrations. In particular, we choose the ‘S calibrator’ from Pilyugin & Grebel (2016) as the fiducial one for this work, to determine the O abundances of all nebular regions. The ‘S calibrator’ is chosen because it is the only calibrator in the MUSE spectral range that estimates metallicity taking into account the dependence of line ratios on both T_e and ionization parameter. The ‘S calibrator’ uses the intensities of the following strong lines: H β , H α , [O III] λ 4959 + λ 5007, [N II] λ 6548 + λ 6584, and [S II] λ 6717 + λ 6731.

The [O III] λ 4959 line for some of the regions, especially in the disc, is only marginally detected. However, the flux of this line is theoretically one third of the [O III] λ 5007 line flux (see e.g. Pérez-Montero 2017). Hence, for the sake of consistency, for all regions we estimated the [O III] λ 4959 line flux from the [O III] λ 5007, using

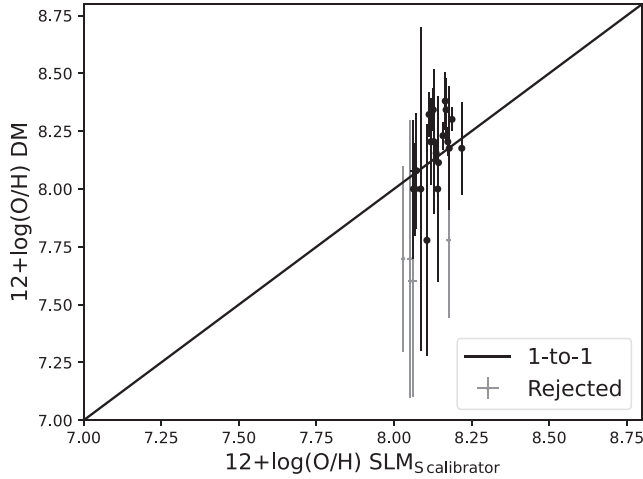


Figure 6. left-hand panel: O abundance with the DM versus that obtained with the S calibrator from Pilyugin & Grebel (2016); right-hand panel: Temperature of the high ionization zone, T_e^{high} , versus $\log N_{2H\beta}$ index, $\frac{[N\text{II}]\lambda 6548 + \lambda 6584}{H\beta}$. The solid line is the tight relation reported in Pilyugin & Grebel (2016); the grey dashed line is the same relation shifted upwards by 5000 K. Estimated T_e^{high} for regions above the dashed line are unlikely to be reliable and hence are rejected (grey points) from the abundance analysis using the DM.

this constant factor. We have derived the O abundance with this method for 152 regions in the external ring, and for 36 regions within the disc. Our results are included in the supplementary MRT table.

In Fig. 6 (left-hand panel) we compare the O abundances obtained using the DM and the S calibrator for the H II regions in the outer ring. The unit-slope line passes through the majority of the points within the calculated errors, implying a general agreement in the abundances determined from the two methods. However, the $12 + \log \frac{O}{H}$ values obtained from DM of 5 regions (shown in grey) are below 8.0, the minimum value obtained from SLM. The inferred low metallicities could be due to overestimation of temperature. In order to investigate this, we plot in Fig. 6 (right-hand panel) the temperature of the high ionization zone, T_e^{high} , versus $N_{2H\beta}$ index ($N_{2H\beta} = \frac{[N\text{II}]\lambda 6548 + \lambda 6584}{H\beta}$). Pilyugin & Grebel (2016) have found the $N_{2H\beta}$ ratio to be a good indicator of temperature. We plot their relation in this plot by a solid line. We also indicate in this plot a line that corresponds to an upward offset of 5000 K as compared to the Pilyugin & Grebel (2016) relation. The same regions for which the inferred $12 + \log \frac{O}{H} < 8.0$ also have the measured temperatures that are higher by as much as 5000 K, as compared to the expected relation.

Recently, Menacho et al. (2021) reported similar O abundance discrepancies between the DM and SLM in some regions of the interacting galaxy Haro 11. They argued that the presence of shocks can overestimate the temperature determination due to a non-Maxwellian distribution of electron velocities (McKee & Hollenbach 1980), or due to the increase of the flux of auroral lines used for the temperature determination (Peimbert, Sarmiento & Fierro 1991). As illustrated in Fig. 5, there is no direct evidence for the presence of shocks in the Cartwheel H II regions, and hence the origin of this discrepancy possibly requires a different explanation.

Arellano-Córdova & Rodríguez (2020) have demonstrated that the O abundances determined from DM tend to be underestimated by more than 0.2 dex for high excitation regions, when using T_e relations to obtain T_e^{high} rather than obtaining it directly from [O III] $\lambda 4363$ line. This is due to the large dispersion in the relations given by equations (2) and (3). Unfortunately, the accuracy of O abundances obtained using T_e ([S III]) remains unexplored. So

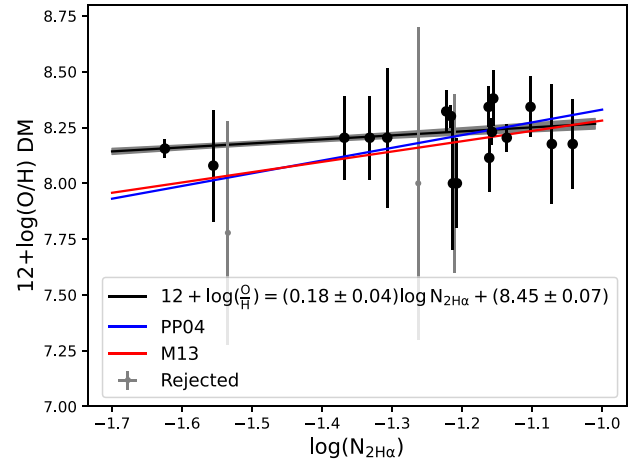
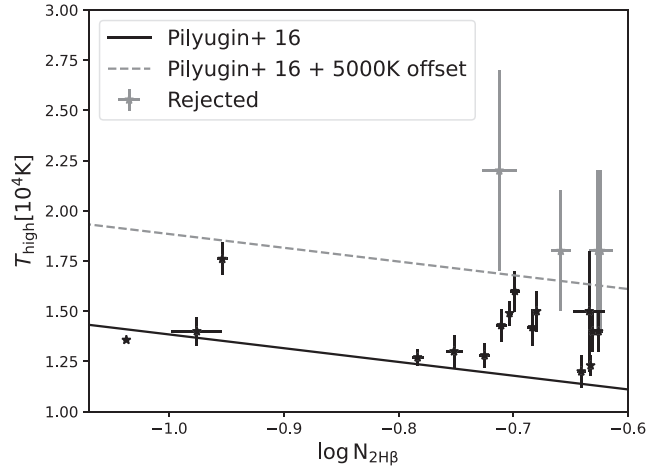


Figure 7. O abundance $12 + \log(O/H)$ determined with the DM versus the $N_{2H\alpha} = \frac{[N\text{II}]\lambda 6548 + \lambda 6584}{H\alpha}$ index for regions from the outer ring of Cartwheel. We plot as solid line our empirical calibration as the error weighted fit; grey points are rejected due to their large relative error. We include the calibrations from Pettini & Pagel (2004) (PP04) and Marino et al. (2013) (M13) as blue and red lines, respectively.

we believe the abundances from DM that have the determined temperature exceeding 5000 K from that expected using the $T_e - N_{2H\beta}$ relation from Pilyugin & Grebel (2016) are not reliable, and hence we discarded all these regions from the DM. We show the rejected regions as grey dots in Fig. 6. When taking into account only the black points, the dispersion of the DM around the S calibrator is ~ 0.1 dex, which is the expected value for SLM calibrations.

In addition, we have estimated our own calibration using the abundances from DM and the value of $N_{2H\alpha} = \frac{[N\text{II}]\lambda 6548 + \lambda 6584}{H\alpha}$. We show in Fig. 7 the O abundance versus the $N_{2H\alpha}$ ratio for the regions in the outer ring. We estimated our O abundance empirical calibration performing a linear error weighted fit:

$$12 + \log\left(\frac{O}{H}\right) = (0.18 \pm 0.04) \log(N_{2H\alpha}) + (8.45 \pm 0.07). \quad (4)$$

The resulting fit is slightly flatter than the N2 calibrations of Pettini & Pagel (2004) (N2-PP04), Marino et al. (2013) (N2-M13).

In order to compare between different empirical calibrations with the fiducial one (S calibrator) and with the one obtained in this work for the regions in the outer ring of Cartwheel (N2-Cartwheel), we also estimate the O abundance using the calibrations from N2-PP04 and N2-M13. The O abundances determined using different empirical calibrations are discussed below.

4 DISCUSSION

We determined O, N, Fe, and He abundances with the DM for 20, 20, 17, and 9 regions, respectively; with the temperature-sensitive line [S III] λ 6312 detected. These regions are located in the outer star-forming ring. The median values for the different abundances are $12 + \log \frac{\text{O}}{\text{H}} = 8.19 \pm 0.15$, $\log \frac{\text{N}}{\text{O}} = -1.57 \pm 0.09$, $\log \frac{\text{Fe}}{\text{O}} = -2.24 \pm 0.09$, and $12 + \log \frac{\text{He}}{\text{H}} = 10.90 \pm 0.03$. The relative abundance of $\frac{\text{N}}{\text{O}}$ is commonly approximated by $\frac{\text{N}}{\text{O}} \approx \frac{\text{N}^+}{\text{O}^+}$. We corroborate that our estimate $\log \frac{\text{N}^+}{\text{O}^+} = -1.56 \pm 0.09$ is consistent with the median value of $\frac{\text{N}}{\text{O}}$ we found.

O, N, and Fe are ejected into the ISM over different time-scales, which allows us to use the measured abundances to determine the nature of the expanding ring wave of star formation in the Cartwheel. The O is mainly enriched in the ISM during the explosive death of massive stars during the core-collapse SNe, which also produce some amount of Fe (Edmunds & Pagel 1978; Pantelaki, Willson & Guzik 1988; Garnett 1990). Slightly prior to this event, the massive stars ($\geq 25 M_{\odot}$) during their Wolf-Rayet (WR) phase ($\sim 2-4$ Myr) can also enrich He, N, and C due to the high mass-loss ($\sim 10^{-4}-10^{-5} M_{\odot} \text{ yr}^{-1}$) through strong stellar winds (Maeder 1992; Crowther 2007). The N has two possible origins, either in massive stars in a ‘secondary way’ using the C and O already present in the star at birth, or in a ‘primary way’ using the freshly produced C and O and dredged up during the AGB phase (Renzini & Voli 1981; Villas-Costas & Edmunds 1993). On the other hand, most of the Fe in the ISM comes from the Type Ia SNe over slightly longer time-scales (Matteucci & Greggio 1986).

The WR star phase and core-collapse SNe explosions occur during the typical lifetime of H II regions and hence nebular O, Fe, N, and He abundances can have contribution from the recently expelled elements. This fact has motivated several authors to look for local enrichment of He/H and N/O ratios in H II regions (see e.g. Pagel, Terlevich & Melnick 1986; Pagel et al. 1992; Kobulnicky et al. 1997). The results of these searches have been mixed so far with reports of local enrichment in the nearby starburst NGC 5253 (López-Sánchez et al. 2007) and in a sample of WR galaxies (Brinchmann, Kunth & Durret 2008) and inconclusive evidence in Mrk 178 (Kehrig et al. 2013). Tenorio-Tagle (1996) argued that the expelled material in the stellar winds and SN ejecta could be trapped in hot coronal gas that would take $\sim 10^8$ yr to cool down enough and allow an efficient mixing of the fresh elements with their local environment. The reason for non-enrichment could also be because some of the processed material can escape the star-forming zone during the SN explosions (Recchi et al. 2004). Under these scenarios, the observed nebular abundances trace the metallicity of the ISM before the formation of the current generation of massive stars. In fact, the abundance could be even less than that of the pre-collisional disc if there is infall of metal-poor gas (Köppen & Hensler 2005).

4.1 Fe/O, N/O versus O/H abundances

Oxygen produced in stars is returned to the ISM and mixed with the ambient cooler gas over relatively short time-scales (a few \times

10^7 yr) as compared to the enrichment of N and Fe (a few $\times 10^8$ yr). Rings of ring galaxies fade over a time-scale of a few $\times 10^8$ yr. In the classical ‘expanding density wave’ models of ring galaxies, the location of star-forming ring moves outward in time, leaving behind the products of SF, i.e. the recently processed elements, at inner radii (e.g. Korchagin, Mayya & Vorobyov 2001). The presently observed star forming ring contains stars formed over the past 10 Myr only, which is too short a period for the enrichment of even O. Hence, the ring H II regions are expected to trace the metallicity of the pre-collisional disc at the current location of the ring (see e.g. Bransford et al. 1998). The metallicity at the ring could be even less than that of the pre-collisional disc if there was an infall of metal-poor gas during the collisional event that triggered the ring formation.

Renaud et al. (2018), who took into account gas dynamics at parsec scales in their recent simulation of ring galaxies, find results that differ qualitatively and quantitatively from the expectations of the classical ‘expanding density wave’ scenario. The gas is swept by the rapidly expanding wave which takes along with it all the products of SF. Recent simulations by Kouroumpatzakis et al. (2021) also support this idea. Under this ‘expanding material-wave’ scenario, the ring contains most of the elements formed in the expanding wave. Furthermore, this model predicts time-scale of ~ 100 Myr for the ring in the Cartwheel. This time-scale is long enough for the expulsion and enrichment of O in the ISM from the stars formed in the wave, but short enough for the enrichment of primary N and Fe produced in SNIa (Recchi et al. 2006). The production of the secondary N in massive stars becomes efficient at $12 + \log \frac{\text{O}}{\text{H}} \geq 8$ (Vincenzo et al. 2016), which suggests that the highest metallicity Cartwheel H II regions could have a relatively higher N/O ratio.

The trends in metallicity expected under the two scenarios of the ring formation described above are different. In the ‘expanding density wave’ scenario, enrichment of O due to SF triggered by the ring wave is expected to occur throughout the disc, with some enrichment of N and Fe at the inner most radii. The ring is not expected to show any metal inhomogeneity. Under this scenario, the variation in the O abundance in the ring H II regions can only arise due to different amount of metal-poor infalling gas in different parts of the ring. However, gas infall would not change the N/O and Fe/O ratios and hence these ratios are expected to be independent of the O/H variation. On the other hand, in the ‘expanding material-wave’ scenario, each H II region contains gas that was enriched by metals expelled from stars over all radii, and hence ages, since the wave started to expand. An azimuthal zone that received material from intense past bursts is expected to have higher O/H as compared to a zone which has not received any metal-enriched gas. The N/H and Fe/H values in the ring H II regions are not expected to deviate much from their pre-collisional values because of the time (~ 100 Myr) elapsed since the ring-making collision is shorter than the typical time-scale required to enrich N and Fe through the primary process. Thus, N/O and Fe/O are expected to systematically decrease as O/H increases. The slope of the relation would depend on the relative contribution of the secondary process in massive stars to the production of N and Fe, with the slope close to unity if the entire N and Fe is of secondary origin in stars less massive than $8 M_{\odot}$. The production of the secondary N in massive stars becomes efficient at $12 + \log \frac{\text{O}}{\text{H}} \geq 8$ (Vincenzo et al. 2016), which suggests that the highest metallicity Cartwheel H II regions could have a relatively higher N/O ratio.

We show the N/O (top) and Fe/O ratios (bottom) versus $12 + \log(\text{O}/\text{H})$ abundances for all the H II regions with T_e measurements in Fig. 8. We see a systematic decrease of both N/O and Fe/O with O/H, which is inconsistent with the trend expected from the ‘expanding density wave’ scenario, but in agreement with the trend

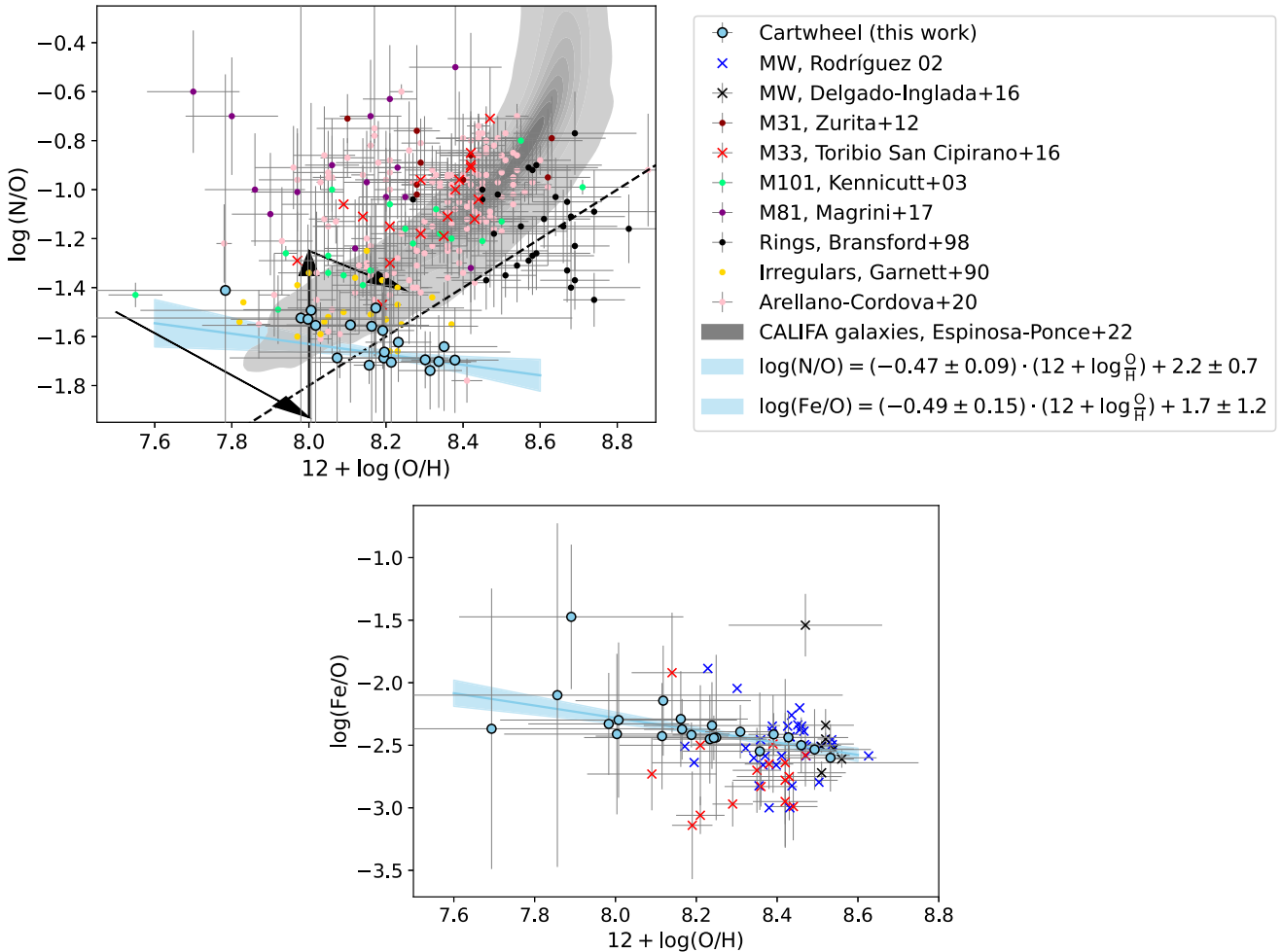


Figure 8. $\log(N/O)$ (top) and $\log(Fe/O)$ (bottom) versus $12 + \log(O/H)$ derived in this work for the Cartwheel ring H II regions using the DM (blue circles) compared with the corresponding values for H II regions in nearby irregular and galaxies compiled from the literature: Irregulars (yellow dots; Garnett 1990); M 101 (green dots; Kennicutt et al. 2003); M 31 (dark red dots; Zurita & Bresolin 2012); M 33 (red crosses; Toribio San Cipriano et al. 2016); M 81 (purple dots; Magrini, Gonçalves & Vajgel 2017); regions of collisional ring galaxies (black dots; Bransford et al. 1998) and regions from different nearby galaxies in Arellano-Córdova & Rodríguez (2020) (pink dots) and Espinosa-Ponce et al. (2020) (grey area). The vectors and the dashed line shown in the top panel are taken from the schematic representation of the evolution of the N/O ratio for a dwarf galaxy from Garnett (1990); The bottom panel includes measurements for the Milky Way (MW) H II regions (blue and black crosses, respectively; Rodríguez 2002; Delgado-Inglada et al. 2016). The blue lines are the error weighted linear fits to the Cartwheel data points, while the shaded area represents the $1 - \sigma$ uncertainty range of the fits.

expected from the alternative scenario of the ‘expanding material-wave’. The slopes of the linear fits to the observed relation (blue lines) are close to 0.5, which suggests non-negligible secondary contribution to N and Fe production from stars more massive than $8M_{\odot}$ in the Cartwheel.

In Fig. 8, we also compare the location of the Cartwheel ring H II regions with that of H II regions in other galaxies. The comparison sample for N/O includes H II regions in nearby spiral galaxies, irregular galaxies, and H II regions in collisional ring galaxies analysed by Bransford et al. (1998). The Cartwheel H II regions span ~ 0.6 dex range in O/H at the low-metallicity end. The N/O values in the Cartwheel H II regions are among the lowest values in the comparison sample. The trend of N/O ratio in the Cartwheel is consistent with the trend seen for irregular galaxies and a few regions in M101. The rest of the galaxies, including the relatively metal-rich ring galaxies studied by Bransford et al. (1998), show N/O enhancements by as much as 0.5–1.0 dex over the values found for the high-metallicity Cartwheel regions. This suggests that the outer

disc of the pre-collisional Cartwheel is chemically less evolved as compared to other ring galaxies.

Data on the Fe abundance for extragalactic H II regions are scarce beyond the Local group, given the faintness of the Fe lines in H II regions. Hence, we compare the results with H II regions in M 33 (Toribio San Cipriano et al. 2016) and the Galactic H II regions (Rodríguez 2002; Delgado-Inglada et al. 2016). These data cover Fe/O ratios only for $12 + \log(O/H) \gtrsim 8.05$. The Fe/O ratio reported here for the Cartwheel galaxy is in agreement with those observed in the Galactic H II regions and M 33. Unfortunately, there are no measurements of Fe/O in low metallicity H II regions in nearby galaxies to compare with.

4.2 Azimuthal variation of O using SLM

The star-forming ring of the ring galaxies shows considerable azimuthal variation in the distribution of intensity in most bands (see e.g. Madore, Nelson & Petrillo 2009, Fig. 5). The Cartwheel

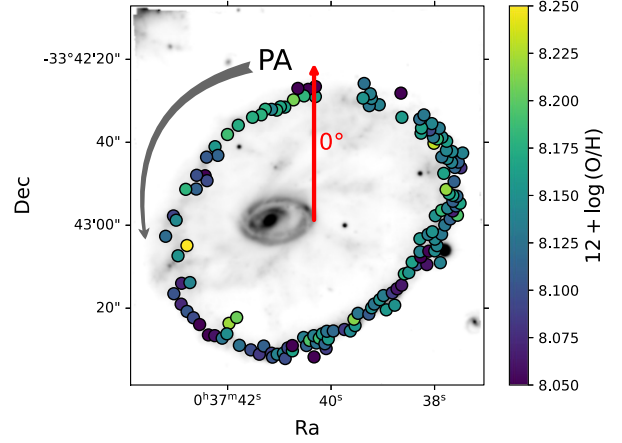
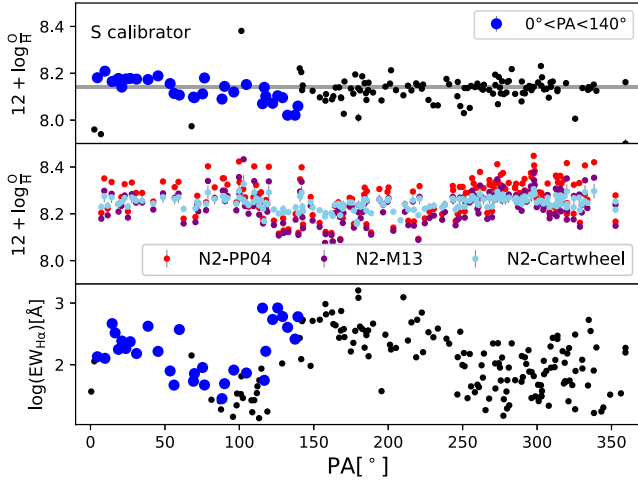


Figure 9. Left-hand panel: O abundances using the S-calibrator versus PA in the external ring of Cartwheel. The azimuthal behaviour for other SLMs are shown in the middle left-hand panel: N2-PP04 (red), N2-M13 (purple), and N2-Cartwheel (light blue). We also plot the EW(H α) versus PA (bottom panel). Regions between 0 and 140 degrees in PA are shown in blue. The grey horizontal line is the median O abundance value for the S calibrator. Right-hand panel: SDSS r -band image of the Cartwheel indicating the O abundance values derived with the S calibrator (colour points). The grey arrow indicates the positive direction starting from PA = 0° (red arrow).

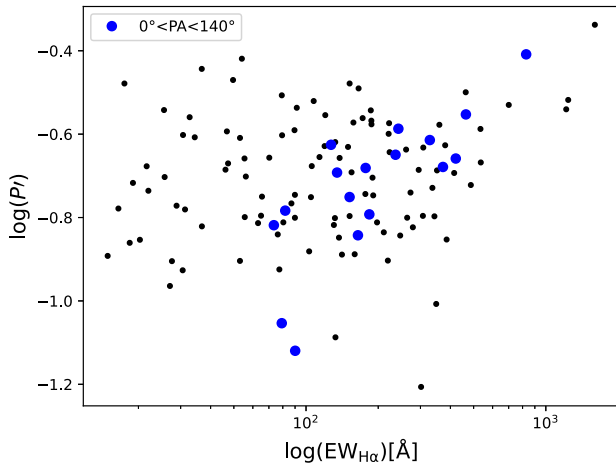


Figure 10. Excitation parameter (P') versus EW(H α). Regions between 0 and 140 degrees in PA (as seen in Fig. 9) are displayed in blue.

is no exception, with the southern half of the ring being noticeably brighter in all bands (see e.g. Marcum et al. 1992; Mayya et al. 2005). This brightness is due to enhanced SF in this part of the ring (Higdon 1995). The distribution of the atomic and molecular gas also shows considerable azimuthal structures (Higdon 1996; Higdon et al. 2015). The azimuthal asymmetry is believed to be due to the non-central impact point of the intruder (e.g. Renaud et al. 2018).

It is of interest to explore the azimuthal variation of O abundances of the ring H II regions. With this purpose, we plot O abundance as a function of PA of the H II regions in the ring in Fig. 9 (left-hand panel). For measuring the PA, we used the centre of the ellipse that best matches the star-forming ring (ellipse #9 in Fig. 11) instead of the nucleus. This centre, $\alpha = 0^{\text{h}}37^{\text{m}}40.27^{\text{s}}$; $\delta = -33^{\circ}42'59.06''$, is illustrated on the SDSS r -band image extracted from the MUSE cube in the right-hand panel of Fig. 9. The O abundance values using the S calibrator are shown in colour for all the ring H II regions using the code in the colour-bar on the right.

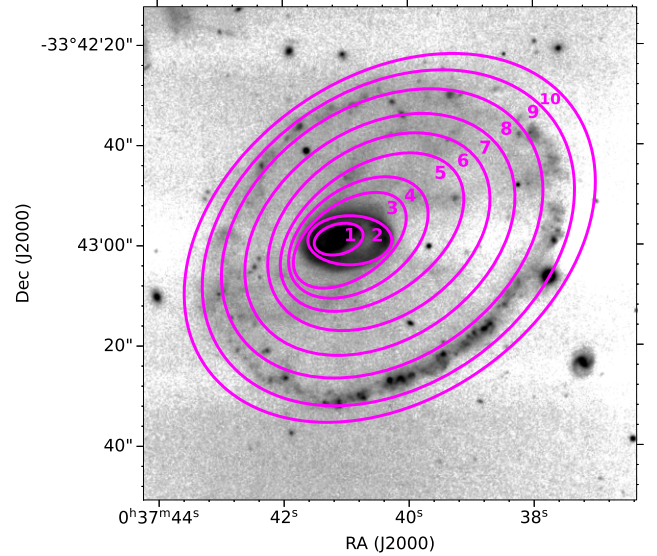


Figure 11. K -band image from Barway et al. (2020) of the Cartwheel galaxy. We show the ten different ellipses (magenta) used to estimate the radius depending on the position in the Cartwheel galaxy.

The O abundance for the majority of the H II regions using the S-calibrator lies close to the median value of $12 + \log(\text{O}/\text{H}) = 8.14$ (grey line in the top left-hand panel of Fig. 9), with a spread of ~ 0.1 dex, which is the typical error of the calibration. However, in the PAs between 0° and 140°, a systematic azimuthal gradient is noticeable. The $12 + \log(\text{O}/\text{H})$ value decreases gradually by 0.2 dex in this 140° azimuthal range. We indicate these regions as blue circles in Fig. 9 (top left-hand panel). In order to explore whether the observed azimuthal gradient is real, or an artefact of the use of SLM, we plot in the middle panel the O abundance calculated using other three SLM calibrators: N2-Cartwheel (light blue; this work), N2-PP04 (red), and N2-M13 (purple). None of these calibrators show the systematic variation between 0° and 140°. Thus, it is likely

that the systematic variation using the S-calibrator is due to some other physical effect that affects the S-calibrator more than other calibrators. The $H\alpha$ EW plotted in the bottom left-hand panel also shows a systematic decrease in the same azimuthal range. The $H\alpha$ EW decreases with age (Leitherer et al. 1999) and hence the high EW regions are expected to be systematically younger by ~ 5 – 10 Myr as compared to low EW regions. There is no reason to believe these relatively older regions are metal-poor as compared to their younger counterparts. On the other hand, the ionization parameter decreases with age, and hence the observed ~ 0.2 dex decrease of the O abundance in the 0° – 140° azimuthal range could be due to the inadequacy of the S-calibrator over the entire observed range of the ionization parameter. We indeed observe a systematic decrease of the ionization parameter, defined as, $P' = \frac{I(\text{S[III]}\lambda 9069)}{I(\text{S[III]}\lambda 9069) + I(\text{S[III]}\lambda 6717 + 31)}$, in the azimuthal range (PAs = 0° – 140°) where the $H\alpha$ EW decreases. In Fig. 10, we plot P' versus $H\alpha$ EW for all the ring regions. The P' for regions in the 0° – 140° azimuthal range (shown as blue dots) clearly correlates with $H\alpha$ EW. This confirms that the S-calibrator we have used does not take into account the age-dependent variation of the ionization parameters in the Cartwheel H II regions. It seems the N2-calibrators are less affected by the cluster evolution. We ignore any intrinsic correlation between ionization parameter and metallicity in H II regions (e.g. Kewley, Nicholls & Sutherland 2019, and references therein), and conclude that we do not have compelling evidence for azimuthal variation of O abundance in the Cartwheel.

4.3 Radial abundance gradient of O

SLM empirical calibrations allowed us to trace the O abundances of the region between the nucleus and the outer ring, which enables for the first time, the determination of the abundance gradient in the disc of the Cartwheel. Obtaining the abundance gradient requires the estimation of galactocentric distances for each $H\alpha$ -emitting region. Under the collisional scenario, ring galaxies have two centres: one defined by the position of the nucleus; the other by the impact point of the intruder galaxy, defined as the centre of the ellipse that best fits the star-forming ring. Pre- and post-collisional gradients, if present, are expected to be symmetric around the nucleus and the impact point, respectively. In order to measure the colour gradients in the Cartwheel, Marcum et al. (1992) proposed a scheme wherein they changed the centre of symmetry smoothly from the nucleus at small radii to the impact point at large radii. We followed their scheme and defined ten different ellipses, which are shown in Fig. 11. The PA and ellipticity of the two innermost ellipses are dictated by the bar and the inner ring. For the subsequent ellipses, the PA is fixed at the value corresponding to that of the outer ring, whereas the ellipticity was decreased gradually from the inner to outer ellipses. We took the semimajor length of the ellipse as the galactocentric distance of the corresponding ellipse. For each region where we measured the O abundance using the SLM, we determined its galactocentric distance by assigning the parameters of the ellipse that passes through the region.

We plot the radial distribution of the O abundances in Fig. 12, where we show each region in the disc as black points and those in the ring as red points. We plot the radial distribution for the fiducial empirical calibration mentioned above: S-calibrator. We also show

⁶We labelled the ionization parameter as P' to distinguish from the more commonly used $P = \frac{I(\text{O[III]}\lambda 4959 + 5007)}{I(\text{O[III]}\lambda 4959 + 5007) + I(\text{O[II]}\lambda 3727 + 29)}$, which cannot be defined for the MUSE data set due to the non-coverage of the $\text{O[II]}\lambda 3727 + 29$ line.

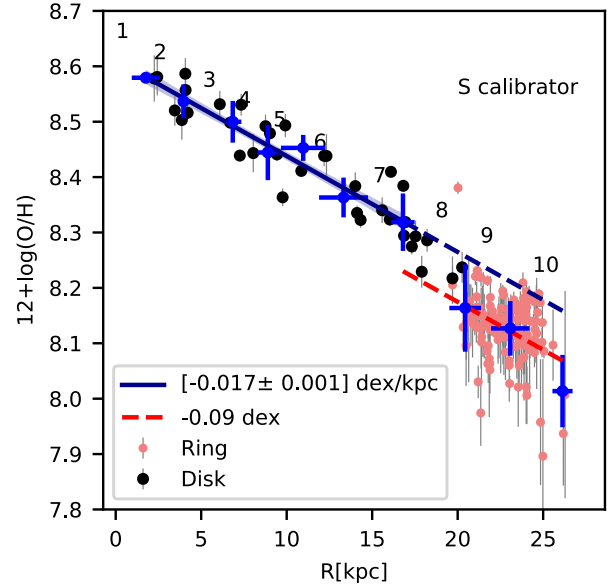


Figure 12. $12 + \log(\text{O}/\text{H})$ versus the radius (R) for the fiducial empirical calibration: S-calibrator (Pilyugin & Grebel 2016). The black points are regions identified in the disc, while red points are those identified in the ring. The blue points are the average values for the regions inside each ellipse (labelled with the number of the ellipse), while the blue line is the fit to the average values of the first seven ellipses and the blue shaded region is the $1-\sigma$ uncertainty range of the fit. We show as a blue dashed line the extrapolation of the linear fit to larger radius, while as a red dashed line the same line, but shifted downwards by -0.09 dex.

the average values for the regions between two consecutive ellipses by blue crosses, where the horizontal and vertical sizes represent the standard deviation of points enclosed by each of our ten ellipses. Clearly defined abundance gradient can be seen in the zone between the inner and the outer ring. We have fitted the average values (blue crosses) of the first seven ellipses by a straight line, which is shown as a continuous blue line. The measured abundances of almost all the regions in the outer ring are systematically lower than the value expected from the extrapolation of the fit, which is shown by a blue dashed line. We find that the abundances of ring regions are consistent with the slope of the fit to the disc regions, but shifted downwards by -0.09 dex. The value of the gradient is -0.017 ± 0.001 dex kpc^{-1} . Assuming $R_{25} = 24.95$ kpc (HyperLeda database; Makarov et al. 2014), which is just at the outer edge of the outer ring, the gradient is equivalent to a value of -0.42 ± 0.03 dex/ R_{25} .

Since O abundance can depend on the assumed empirical calibration, we also show in Fig. 13 the gradient for the three different empirical calibrations discussed above: N2-Cartwheel (upper; this work); N2-PP04 (middle), and N2-M13 (bottom). The two basic characteristics found using the S-calibrator, namely a negative abundance gradient and the downward shift in abundance in the ring, are seen for all the three N2-calibrator relations. The values of the gradient and the shift obtained for the N2-M13 and N2-PP04 calibrators agree within each other, with mean values of gradient ~ -0.008 dex kpc^{-1} and shift $= -0.15$ dex. This gradient is around a factor of two shallower and the shift 66 per cent larger, as compared to that of the S-calibrator. The N2-Cartwheel calibration has been obtained using the regions in the outer ring. The extrapolation of this calibration to the regions in the inner disc is probably incorrect due to the systematically lower ionization parameter of the inner

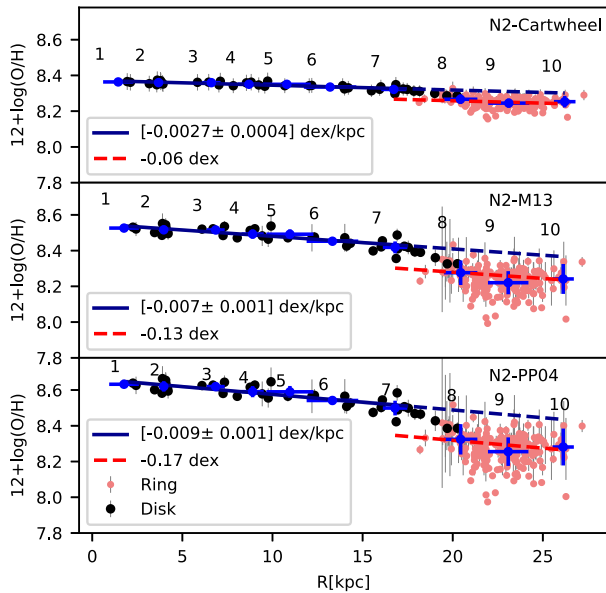


Figure 13. $12 + \log(\text{O}/\text{H})$ versus radius (R). We plot the O abundance for three empirical calibrations: N2-Cartwheel (top panel; this work); N2-M13 (middle; Marino et al. 2013) and N2-PP04 (bottom; Pettini & Pagel 2004). The black points are regions identified in the disc, while red points are those identified in the ring. The blue points are the average values for the regions inside each ellipse (labelled with the number of the ellipse), while the blue line is the fit to the average values of the first seven ellipses and the blue shaded region is the $1-\sigma$ uncertainty range of the fit. We show as a blue dashed line the projection of the linear fit to larger radius, while as a red dashed line the same projection although shifted downwards by factor which depends on the empirical calibration used.

disc regions, which is most likely the reason for its discrepancy with respect to the other two N2 calibrators.

The difference between methods is consistent with that reported by Zurita et al. (2021) for 2831 H II regions in nearby galaxies.

The slope using the fiducial calibrator is steeper compared with those of normal galaxies reported in Pilyugin et al. (2019) ($-0.158 \text{ dex}/R_{25}$). Assuming an effective radius of $r_e = 5.13 \text{ kpc}$ (J band; Skrutskie et al. 2006), the slope is $-0.087 \pm 0.005 \text{ dex}/r_e$ for the S calibrator. The gradient is in agreement with those found for normal galaxies from different surveys such as CALIFA ($-0.07 \pm 0.05 \text{ dex}/r_e$; Sánchez-Menguiano et al. 2016), MANGA ($-0.07 \pm 0.1 \text{ dex}/r_e$; Belfiore et al. 2017), and AMUSING ($-0.1 \pm 0.03 \text{ dex}/r_e$; Sánchez-Menguiano et al. 2018), see Sánchez (2020) for a review. The gradients estimated using the N2 calibrators are slightly shallower, as those normally found in interacting galaxies (Rupke, Kewley & Chien 2010; Sánchez et al. 2014). However, since we are dealing with regions with very different ages and excitation parameters in the inner disc and the outer ring, the gradient value obtained using the fiducial S-calibrator is more trustworthy.

The observed agreement of the gradient in the Cartwheel with that in the normal galaxies over the characteristic radii R_{25} and r_e would suggest that the star formation in the disc of the Cartwheel following the ring-producing interaction has not resulted in noticeable change in its abundance properties in the inner disc, assuming the R_{25} and r_e have not undergone changes due to interaction. The downward shift of the O abundance in the ring regions is present (although with different values) in all the calibrations. Therefore, the existence of an abundance shift in the outer ring is rather convincing.

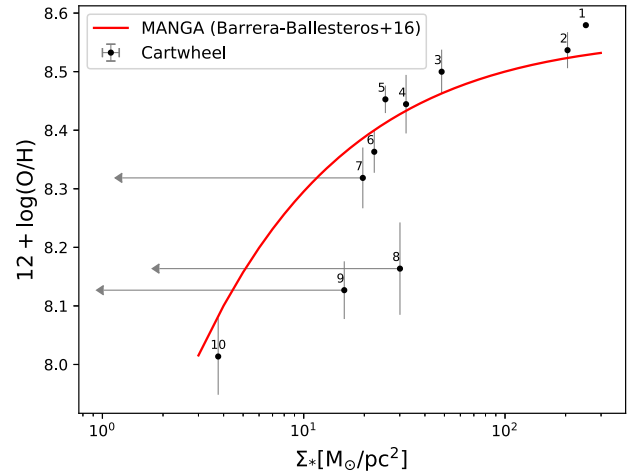


Figure 14. $12 + \log(\text{O}/\text{H})$ versus the stellar mass surface density (Σ_*). We show as black dots the points for the 10 ellipses defined in Cartwheel (labelled with the number of the ellipse). Ellipses 7, 8, and 9 are affected by young stellar component contamination. The arrows represent the maximum effect of this contamination. We show as a red line the metallicity– Σ_* relation reported by the MANGA survey (Barrera-Ballesteros et al. 2016).

4.4 Stellar mass surface density versus metallicity relation

Metals expected from stars formed by the passage of the expanding density wave are expected to contribute to the creation of metallicity gradient (e.g. Korchagin et al. 1999). However, to establish whether or not the observed gradient in the Cartwheel is created by the expanding wave, a knowledge of the gradient in its pre-collisional disc is required. Metallicity in a galaxy is related to the mass in old stars, e.g. Maiolino & Mannucci (2019) and references therein. The stellar mass for the Cartwheel was determined using the K -band total flux and a mass-to-light ratio appropriate to the disc of the Cartwheel. We used the K -band image from Barway et al. (2020) to obtain a total flux from old stars by masking all bright H II regions. We obtained $K = 11.50$, which is in good agreement with the measurement of $K = 11.55$, reported by Marcum et al. (1992). We used $\log(\frac{M}{L_K}) = -0.2$ from Bell et al. (2003) corresponding to a disc colour of $B - V = 0.4$ and $M_{K\odot} = 3.33$, to obtain a $\log(M_*/M_\odot) = 10.75$ for the Cartwheel. For this mass, normal disc galaxies are expected to have a gradient of $\sim -0.01 \text{ dex}/\text{kpc}$ (Pilyugin et al. 2019), which is marginally shallower than the gradient obtained for the Cartwheel. In order to explore further the origin of the gradient, we carry out a spatially resolved analysis of the stellar mass surface density (Σ_*) versus metallicity relation. A local relation between these two quantities has been found in normal spiral galaxies (Rosales-Ortega et al. 2012). Anomalies from this local relation are observed and associated to gas accretion, for example due to galaxy interactions (Hwang et al. 2019; Sánchez-Menguiano et al. 2019). We compare the average abundance for all the regions in the zone enclosed by successive ellipses with the azimuthally averaged Σ_* , determined from the corresponding K -band surface brightness and using the $\log(M/L_K)$ mentioned above.

We compare Σ_* with $12 + \log(\text{O}/\text{H})$ in Fig. 14 for each of the elliptical annulus. We show the results for the Cartwheel galaxy as black stars and compare these points with the relation reported by the MANGA survey (Barrera-Ballesteros et al. 2016). The points for the inner six ellipses and to some extent the outer-most ellipse, are in excellent agreement with Σ_* –metallicity relation for normal galaxies observed by the MANGA survey. On the other hand, the points for ellipses #7, #8, and #9 are too metal-poor for their stellar content,

or too bright for their observed (low) metallicity. Ellipse #9 encloses the star-forming ring, where our assumption that all the K -band flux comes from old stars clearly overestimates the stellar mass. Ellipses #8 and #7 are in the wake of the expanding wave and hence the regions in these annuli are expected to contain descendants of massive stars, especially the red supergiants (RSGs) which could contribute substantially to the observed K -band surface brightness. We hence obtained an alternative value of stellar surface density assuming that the entire observed K -band surface brightness originates in RSGs. For this purpose we used a $\log(M/L_K) = -1.2$ from Eldridge et al. (2017) models for a 6 Myr population. These are indicated by the arrows. The real Σ_* is expected to be somewhere between these two extreme cases, depending on the relative contribution of wave-induced star formation and pre-collisional disc stars to the K -band surface brightness. The sizes of the arrows are consistent with this scenario of contamination of the K -band SB of ellipses #7, #8, and #9 from wave-induced SF and hence the observed slope of the metallicity gradient in the inner-most six ellipses and the zone outside the star-forming ring represents that of the pre-collisional disc.

4.5 Chemical evolution scenario in the Cartwheel and other ring galaxies

Combining the results of abundance gradient (Fig. 12) with the local mass–metallicity relation (Fig. 14) suggests that the observed abundance gradient in the Cartwheel is inherited from the pre-collisional disc rather than from metals expelled from stars formed by the passage of the expanding wave in the disc. On the other hand, the decrease of N/O and Fe/O with the O abundance implies the presence of recently processed O, but not much of N and Fe, in the ring H II regions. This can be explained as due to the displacement of the O processed in massive stars to the current location of the ring, before the enrichment of primary N and Fe. The age of ~ 100 Myr inferred for the ring of the Cartwheel in recent simulations incorporating parsec-scale hydrodynamical processes by Renaud et al. (2018) is consistent with the chemically constrained age. However, Fig. 12 suggests a clear downward offset in O abundance by ~ 0.1 dex for the ring H II regions with respect to the extrapolation of the gradient of the inner disc. If the ring contains O processed after the ring-making interaction, the O abundance is expected to be higher, rather than lower, than the pre-collisional value. This apparent contradiction can be understood as due to the mixing of the ISM containing the pre- and post-collisional elements in the ring by the gas that is more metal-poor than that of the pre-collisional disc (e.g. Köppen & Hensler 2005). One way of acquiring this metal-poor gas is through gas infall from the intruder, which has to be metal-poor. In the ‘expanding material-wave’ scenario proposed by Renaud et al. (2018), the processed elements are mixed naturally with the accreted metal-poor gas at successively outer radius. Most of the gas mass in the Cartwheel is in the atomic form (Higdon 1996; Higdon et al. 2015), which is concentrated in the outer ring, which supports our hypothesis that dilution of ISM from metal-poor gas is responsible for the lower than the expected metallicity in the ring regions.

In Fig. 15, we show the amount of metal-poor gas that is required to explain the observed downward offset in the abundances of the ring H II regions with respect to that expected in the pre-collisional disc at the location of the outer ring. In this calculation, we assumed no metal-enrichment from the wave-induced SF. We infer that 50 per cent of the presently observed gas mass is of infall origin, if the metallicity of the infalling gas (Z_{in}) is half of that of the pre-collisional disc (Z_{pre}). The infall gas mass percentage could be as

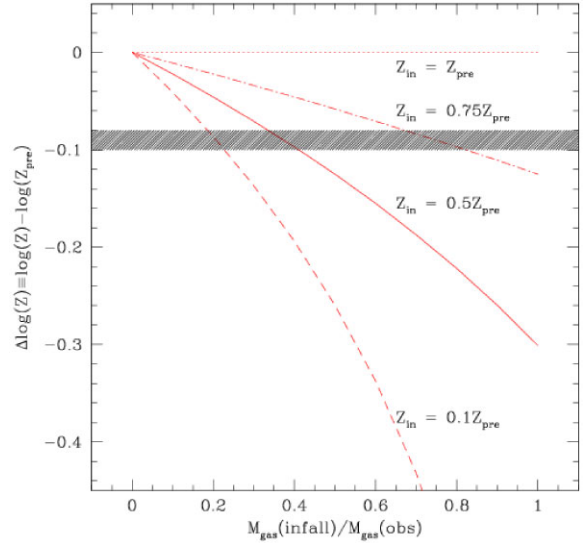


Figure 15. The effect of infall of metal-poor gas on the net metallicity. Curves are plotted for four values of abundance of infalling gas (Z_{in}) in terms of the metallicity of the pre-collisional disc (Z_{pre}). The observed deficit in the metallicity of the ring regions (the horizontal band) requires infall of the metal-poor gas, which constitutes ~ 20 – 70 per cent of the observed gas mass, the exact value depending on the metallicity of the infalling gas.

high as 80 per cent if $Z_{\text{in}} = 0.75 \times Z_{\text{pre}}$, or as low as 20 per cent if $Z_{\text{in}} = 0.1 \times Z_{\text{pre}}$.

4.6 Helium abundance

The average He abundance for the 14 regions where we were able to estimate it is $12 + \log(\text{He}/\text{H}) = 10.90 \pm 0.03$. This value is close to the one found by Fosbury & Hawarden (1977) of $12 + \log(\text{He}/\text{H}) = 10.86$ for the region we are labelling as #99. The value we obtain is also close to the average value of H II regions in M 33 reported by Toribio San Cipriano et al. (2016) of $12 + \log(\text{He}/\text{H}) = 10.98 \pm 0.06$, the average value for H II galaxies reported by Fernández et al. (2018) of $12 + \log(\text{He}/\text{H}) = 10.94 \pm 0.04$, as well as the median value of $12 + \log(\text{He}/\text{H}) = 10.9$ for galaxies with $12 + \log(\text{O}/\text{H}) = 8.0$ from the CALIFA survey (Valerdi 2021), which implies that the enrichment of He has not been peculiar for the Cartwheel galaxy.

5 CONCLUSIONS

We have presented the nebular abundance analysis of 221 H II regions identified in the external ring of the Cartwheel galaxy, as well as 40 regions inside the disc, using the spectroscopic data from the MUSE instrument. We were able to determine the O, N, Fe, and He abundances for a total of 20, 20, 17, and 9 regions, respectively, in the ring using the DM. For the regions in which the temperature sensitive [S III] $\lambda 6312$ line was not detected, we have used the strong-line calibration method from Pilyugin & Grebel (2016) to derive the O abundance in 152 and 24 regions in the external ring and the disc, respectively. These measurements show a systematic radial gradient corresponding to a slope of -0.017 ± 0.001 dex kpc^{-1} , which is consistent with those found in normal spirals (Pilyugin et al. 2019). The observed O abundances in the region between the nucleus and the outer ring follow the well-established local mass surface density–metallicity (Σ_* - $12 + \log(\text{O}/\text{H})$) relation found for normal disc galaxies in the MANGA survey (Barrera-Ballesteros

et al. 2016). This implies that the abundance of elements in the disc of the Cartwheel has little or no contribution from local enrichment from the stars formed by the expanding wave in the past, or its dilution due to radial inflow of metal-poor gas. The empirically derived O abundances drop by ~ 0.1 dex at the ring, which suggests the presence of some amount of metal-poor gas in the ring. We do not find evidence for enrichment of He in the Cartwheel. The abundance trends found in this work are in good agreement with the predictions of transfer of material (gas and recently formed stars) in the expanding wave obtained in recent simulation of the Cartwheel galaxy by Renaud et al. (2018) that takes into account gas-dynamical processes at parsec scales, or scenarios of the formation of ring galaxies in recent cosmological models by Elagali et al. (2018). On the other hand, classical expanding density wave models fail to explain the observed abundance trends.

ACKNOWLEDGEMENTS

This research has made use of the services of the ESO Science Archive Facility (program ID: 60.A-9333), PYNEB (Luridiana et al. 2015), ASTROPY,⁷ a community-developed core Python package for Astronomy (Astropy Collaboration 2013, 2018), APLPY, an open-source plotting package for Python (Robitaille & Bressert 2012), ASTROQUERY, a package that contains a collection of tools to access online Astronomical data (Ginsburg et al. 2019), the MUSE Python Data Analysis (MPDAF; Bacon et al. 2016) and pyregion (<https://github.com/astropy/pyregion>), a python module to parse ds9 region files. We thank the anonymous reviewer for the careful reading of our manuscript and the many insightful comments and suggestions. We also thank CONACyT for the research grant CB-A1-S-25070 (YDM).

DATA AVAILABILITY

The fluxes of principal emission lines used in this work are available in the article and in its online supplementary material. The reduced fits files on which these data are based will be shared on reasonable request to the first author. The ESO datacubes are in the public domain.

REFERENCES

Appleton P. N., Marston A. P., 1997, *AJ*, 113, 201
 Appleton P. N., Struck-Marcel C., 2010, *Fund. Cosmic Phys.*, 16, 111
 Arellano-Córdova K. Z., Rodríguez M., 2020, *MNRAS*, 497, 672
 Astropy Collaboration, 2013, *A&A*, 558, A33
 Astropy Collaboration, 2018, *AJ*, 156, 123
 Bacon R. et al., 2010, in McLean I. S., Ramsay S. K., Takami H., eds, *Proc. SPIE 7735, Ground-based and Airborne Instrumentation for Astronomy III*. SPIE, Bellingham, p. 773508
 Bacon R. et al., 2016, record ascl.soft.1611.003
 Bacon R. et al., 2017, *A&A*, 608, A1
 Baldwin J. A., Phillips M. M., Terlevich R., 1981, *PASP*, 93, 5
 Barrera-Ballesteros J. K. et al., 2016, *MNRAS*, 463, 2513
 Barrera-Ballesteros J. K. et al., 2020, *MNRAS*, 492, 2651
 Barway S., Mayya Y. D., Robleto-Orús A., 2020, *MNRAS*, 497, 44
 Belfiore F. et al., 2017, *MNRAS*, 469, 151
 Belfiore F. et al., 2022, *A&A*, 659, A26
 Bell E. F. et al., 2003, *ApJSS*, 149, 289
 Bittner A. et al., 2019, *A&A*, 628, A117
 Bransford M. A. et al., 1998, *AJ*, 116, 2757

Bresolin F. et al., 2009, *ApJ*, 700, 309
 Brinchmann J., Kunth D., Durret F., 2008, *A&A*, 485, 657
 Cappellari M., 2017, *MNRAS*, 466, 798
 Cardelli J. A., Clayton G. C., Mathis J. S., 1989, *ApJ*, 345, 245
 Crowther P. A., 2007, *ARA&A*, 45, 177
 Delgado-Inglada G. et al., 2016, *MNRAS*, 456, 3855
 Edmunds M. G., Pagel B. E. J., 1978, *MNRAS*, 185, 77P
 Elagali A. et al., 2018, *MNRAS*, 481, 2951
 Eldridge J. J. et al., 2017, *Publ. Astron. Soc. Austr.*, 34, e058
 Espinosa-Ponce C. et al., 2020, *MNRAS*, 494, 1622
 Esteban C. et al., 2009, *ApJ*, 700, 654
 Fernández V. et al., 2018, *MNRAS*, 478, 5301
 Fosbury R. A. E., Hawarden T. G., 1977, *MNRAS*, 178, 473
 Garnett D. R., 1990, *ApJ*, 363, 142
 Garnett D. R., 1992, *AJ*, 103, 1330
 Ginsburg A. et al., 2019, *AJ*, 157, 98
 Higdon J. L., 1995, *ApJ*, 455, 524
 Higdon J. L., 1996, *ApJ*, 467, 241
 Higdon J. L. et al., 2015, *ApJ*, 814, L1
 Hwang H.-C. et al., 2019, *ApJ*, 872, 144
 Izotov Y. I. et al., 2006, *A&A*, 448, 955
 Izotov Y. I., Stasińska G., Guseva N. G., 2013, *A&A*, 558, A57
 Kauffmann G. et al., 2003, *MNRAS*, 346, 1055
 Kehrig C. et al., 2013, *MNRAS*, 432, 2731
 Kennicutt R. C., Bresolin F., Garnett D. R., 2003, *ApJ*, 591, 801
 Kewley L. J. et al., 2006, *MNRAS*, 372, 961
 Kewley L. J., Nicholls D. C., Sutherland R. S., 2019, *ARA&A*, 57, 511
 Kobulnicky H. A. et al., 1997, *ApJ*, 477, 679
 Köppen J., Hensler G., 2005, *A&A*, 434, 531
 Korchagin V., Vorobyov E., Mayya Y. D., 1999, *ApJ*, 522, 767
 Korchagin V., Mayya Y. D., Vorobyov E., 2001, *ApJ*, 554, 281
 Kouroumpatzakis K. et al., 2021, *MNRAS*, 500, 962
 Leitherer C. et al., 1999, *ApJS*, 123, 3
 López-Sánchez A. R. et al., 2007, *ApJ*, 656, 168
 Luridiana V., Morisset C., Shaw R. A., 2015, *A&A*, 573, A42
 Lynds R., Toomre A., 1976, *ApJ*, 209, 382
 Madore B. F., Nelson E., Petrillo K., 2009, *ApJS*, 181, 572
 Maeder A., 1992, *A&A*, 264, 105
 Magrini L., Gonçalves D. R., Vajgel B., 2017, *MNRAS*, 464, 739
 Maiolino R., Mannucci F., 2019, *A&AR*, 27, 3
 Makarov D. et al., 2014, *A&A*, 570, A13
 Marcum P. M., Appleton P. N., Higdon J. L., 1992, *ApJ*, 399, 57
 Marino R. A. et al., 2013, *A&A*, 559, A114
 Marston A. P., Appleton P. N., 1995, *AJ*, 109, 1002
 Matteucci F., Greggio L., 1986, *A&A*, 154, 279
 Mayya Y. D. et al., 2005, *ApJ*, 620, L35
 McCall M. L., Rybski P. M., Shields G. A., 1985, *ApJS*, 57, 1
 McKee C. F., Hollenbach D. J., 1980, *ARA&A*, 18, 219
 Menacho V. et al., 2021, *MNRAS*, 506, 1777
 Osterbrock D. E., Ferland G. J., 2006, *Astrophysics of Gaseous Nebulae and Active Galactic Nuclei*. University Science Books, CA
 Ott T., 2012, QFitsView: FITS file viewer, record ascl:1210.019
 Pagel B. E. J., Terlevich R. J., Melnick J., 1986, *PASP*, 98, 1005
 Pagel B. E. J. et al., 1992, *MNRAS*, 255, 325
 Pantelaki I., Willson L. A., Guzik J., 1988, *Bull. Am. Astron. Soc.*, 20, 1100
 Peimbert M., Sarmiento A., Fierro J., 1991, *PASP*, 103, 815
 Pérez-Montero E., 2017, *PASP*, 129, 043001
 Pettini M., Pagel B. E. J., 2004, *MNRAS*, 348, L59
 Pilyugin L. S., Grebel E. K., 2016, *MNRAS*, 457, 3678
 Pilyugin L. S. et al., 2019, *A&A*, 623, A122
 Recchi S. et al., 2004, *A&A*, 426, 37
 Recchi S. et al., 2006, *A&A*, 445, 875
 Renaud F. et al., 2018, *MNRAS*, 473, 585
 Renzini A., Voli M., 1981, *A&A*, 94, 175
 Robitaille T., Bressert E., 2012, record ascl.soft.1208.017
 Rodríguez M., 2002, *A&A*, 389, 556
 Rosales-Ortega F. F. et al., 2012, *ApJ*, 756, L31
 Rupke D. S. N., Kewley L. J., Chien L.-H., 2010, *ApJ*, 723, 1255

⁷<http://www.astropy.org>

Sánchez S., 2020, *ARA&A*, 58, 99
 Sánchez S. F. et al., 2014, *A&A*, 563, A49
 Sánchez S. F. et al., 2015, *A&A*, 574, A47
 Sánchez-Menguiano L. et al., 2016, *A&A*, 587, A70
 Sánchez-Menguiano L. et al., 2018, *A&A*, 609, A119
 Sánchez-Menguiano L. et al., 2019, *ApJ*, 882, 9
 Schlafly E. F., Finkbeiner D. P., 2011, *ApJ*, 737, 103
 Skrutskie M. F. et al., 2006, *AJ*, 131, 1163
 Struck C., 2010, *MNRAS*, 403, 1516
 Tenorio-Tagle G., 1996, *AJ*, 111, 1641
 Toribio San Cipriano L. et al., 2016, *MNRAS*, 458, 1866
 Tresse L., Maddox S., Loveday J., Singleton C., 1999, *MNRAS*, 310, 262
 Valerdi M. et al., 2021, *MNRAS*, 505, 5460
 Vazdekis A. et al., 2010, *MNRAS*, 404, 1639
 Villas-Costas M. B., Edmunds M. G., 1993, *MNRAS*, 265, 199
 Vincenzo F. et al., 2016, *MNRAS*, 458, 3466
 Zurita A., Bresolin F., 2012, *MNRAS*, 427, 1463
 Zurita A. et al., 2021, *MNRAS*, 500, 2359

SUPPORTING INFORMATION

Supplementary data are available at [MNRAS](https://academic.oup.com/mnras) online.

ReadMe.dat
table.cartwheel.dat

Please note: Oxford University Press is not responsible for the content or functionality of any supporting materials supplied by the authors. Any queries (other than missing material) should be directed to the corresponding author for the article.

APPENDIX A: SUPPLEMENTARY MATERIAL

An extended version of Table 1 that contains measured fluxes and errors of all the emission lines used in this study is available as a machine readable table for the 252 identified regions in the online version of the article.

Here we list the description of each of the columns present in the MRT table:

1. Identification label.
2. Right Ascension (J2000).
3. Declination (J2000).
4. Electron temperature for the low ionization zone T_e^{low} .
5. Electron temperature for the low ionization zone error.
6. Electron temperature for the high ionization zone T_e^{high} .
7. Electron temperature for the high ionization zone error.
8. Electron temperature for the medium ionization zone T_e^{medium} .
9. Electron temperature for the medium ionization zone error.
10. Electron density N_e estimated from [S II] λ 6717/ λ 6731 lines.
11. Electron density error.
12. Fe III/H abundance ratio.
13. Fe III/H abundance ratio error.
14. O I/H abundance ratio.
15. O I/H abundance ratio error.
16. O II/H abundance ratio.
17. O II/H abundance ratio error.
18. O III/H abundance ratio.
19. O III/H abundance ratio error.
20. N II/H abundance ratio.
21. N II/H abundance ratio error.
22. He I/H abundance ratio.
23. He I/H abundance ratio error.
24. He II/H abundance ratio.
25. He II/H abundance ratio error.

26. Fe/H abundance ratio.
27. Fe/H abundance ratio error.
28. O/H abundance ratio.
29. O/H abundance ratio error.
30. N/H abundance ratio.
31. N/H abundance ratio error.
32. He/H abundance ratio.
33. He/H abundance ratio error.
34. Position Angle (PA) in the ring.
35. *Halpa* Equivalent width.
36. A_V determined from the H α and H β lines.
37. A_V error.
38. Galactocentric radius R_{gal} .
39. Oxygen abundance derived with the strong lines method from Pilyugin & Grebel (2016).
40. Oxygen abundance error derived with the strong lines method.
41. H β Equivalent width.
42. SNR of H β flux.
43. Attenuation-corrected flux of H β .
44. Attenuation-corrected flux error of H β .
45. $100 \times \frac{F_{\text{[Fe III]4659A}}}{F_{\text{H}\beta}}$ ratio.
46. $100 \times \frac{F_{\text{[Fe III]4659A}}}{F_{\text{H}\beta}}$ ratio error.
47. $100 \times \frac{F_{\text{[He II]4686A}}}{F_{\text{H}\beta}}$ ratio.
48. $100 \times \frac{F_{\text{[He II]4686A}}}{F_{\text{H}\beta}}$ ratio error.
49. $100 \times \frac{F_{\text{[Fe III]4701A}}}{F_{\text{H}\beta}}$ ratio.
50. $100 \times \frac{F_{\text{[Fe III]4701A}}}{F_{\text{H}\beta}}$ ratio error.
51. $100 \times \frac{F_{\text{[Ar IV]4711A}}}{F_{\text{H}\beta}}$ ratio.
52. $100 \times \frac{F_{\text{[Ar IV]4711A}}}{F_{\text{H}\beta}}$ ratio error.
53. $100 \times \frac{F_{\text{[Ar IV]4740A}}}{F_{\text{H}\beta}}$ ratio.
54. $100 \times \frac{F_{\text{[Ar IV]4740A}}}{F_{\text{H}\beta}}$ ratio error.
55. $100 \times \frac{F_{\text{[He I]4922A}}}{F_{\text{H}\beta}}$ ratio.
56. $100 \times \frac{F_{\text{[He I]4922A}}}{F_{\text{H}\beta}}$ ratio error.
57. $100 \times \frac{F_{\text{[O III]4959A}}}{F_{\text{H}\beta}}$ ratio.
58. $100 \times \frac{F_{\text{[O III]4959A}}}{F_{\text{H}\beta}}$ ratio error.
59. $100 \times \frac{F_{\text{[Fe III]4986A}}}{F_{\text{H}\beta}}$ ratio.
60. $100 \times \frac{F_{\text{[Fe III]4986A}}}{F_{\text{H}\beta}}$ ratio error.
61. $100 \times \frac{F_{\text{[O III]5007A}}}{F_{\text{H}\beta}}$ ratio.
62. $100 \times \frac{F_{\text{[O III]5007A}}}{F_{\text{H}\beta}}$ ratio error.
63. $100 \times \frac{F_{\text{[He I]5016A}}}{F_{\text{H}\beta}}$ ratio.
64. $100 \times \frac{F_{\text{[He I]5016A}}}{F_{\text{H}\beta}}$ ratio error.
65. $100 \times \frac{F_{\text{[He I]5048A}}}{F_{\text{H}\beta}}$ ratio.
66. $100 \times \frac{F_{\text{[He I]5048A}}}{F_{\text{H}\beta}}$ ratio error.
67. $100 \times \frac{F_{\text{[Fe III]5270A}}}{F_{\text{H}\beta}}$ ratio.
68. $100 \times \frac{F_{\text{[Fe III]5270A}}}{F_{\text{H}\beta}}$ ratio error.
69. $100 \times \frac{F_{\text{[N II]5755A}}}{F_{\text{H}\beta}}$ ratio.
70. $100 \times \frac{F_{\text{[N II]5755A}}}{F_{\text{H}\beta}}$ ratio error.
71. $100 \times \frac{F_{\text{[He I]5876A}}}{F_{\text{H}\beta}}$ ratio.
72. $100 \times \frac{F_{\text{[He I]5876A}}}{F_{\text{H}\beta}}$ ratio error.
73. $100 \times \frac{F_{\text{[O I]6300A}}}{F_{\text{H}\beta}}$ ratio.
74. $100 \times \frac{F_{\text{[O I]6300A}}}{F_{\text{H}\beta}}$ ratio error.
75. $100 \times \frac{F_{\text{[S III]6312A}}}{F_{\text{H}\beta}}$ ratio.
76. $100 \times \frac{F_{\text{[S III]6312A}}}{F_{\text{H}\beta}}$ ratio error.

77. $100 \times \frac{F_{\text{[O II]6364A}}}{F_{\text{H}\beta}}$ ratio.
 78. $100 \times \frac{F_{\text{[O II]6364A}}}{F_{\text{H}\beta}}$ ratio error.
 79. $100 \times \frac{F_{\text{[N II]6548A}}}{F_{\text{H}\beta}}$ ratio.
 80. $100 \times \frac{F_{\text{[N II]6548A}}}{F_{\text{H}\beta}}$ ratio error.
 81. $100 \times \frac{F_{\text{H}\alpha}}{F_{\text{H}\beta}}$ ratio.
 82. $100 \times \frac{F_{\text{H}\alpha}}{F_{\text{H}\beta}}$ ratio error.
 83. $100 \times \frac{F_{\text{[N II]6584A}}}{F_{\text{H}\beta}}$ ratio.
 84. $100 \times \frac{F_{\text{[N II]6584A}}}{F_{\text{H}\beta}}$ ratio error.
 85. $100 \times \frac{F_{\text{[He I]6678A}}}{F_{\text{H}\beta}}$ ratio.
 86. $100 \times \frac{F_{\text{[He I]6678A}}}{F_{\text{H}\beta}}$ ratio error.
 87. $100 \times \frac{F_{\text{[S II]6716A}}}{F_{\text{H}\beta}}$ ratio.
 88. $100 \times \frac{F_{\text{[S II]6716A}}}{F_{\text{H}\beta}}$ ratio error.
 89. $100 \times \frac{F_{\text{[S II]6731A}}}{F_{\text{H}\beta}}$ ratio.
 90. $100 \times \frac{F_{\text{[S II]6731A}}}{F_{\text{H}\beta}}$ ratio error.
 91. $100 \times \frac{F_{\text{[He I]7065A}}}{F_{\text{H}\beta}}$ ratio.
 92. $100 \times \frac{F_{\text{[He I]7065A}}}{F_{\text{H}\beta}}$ ratio error.

93. $100 \times \frac{F_{\text{[He I]7281A}}}{F_{\text{H}\beta}}$ ratio.
 94. $100 \times \frac{F_{\text{[He I]7281A}}}{F_{\text{H}\beta}}$ ratio error.
 95. $100 \times \frac{F_{\text{[O II]7319A}}}{F_{\text{H}\beta}}$ ratio.
 96. $100 \times \frac{F_{\text{[O II]7319A}}}{F_{\text{H}\beta}}$ ratio error.
 97. $100 \times \frac{F_{\text{[O II]7330A}}}{F_{\text{H}\beta}}$ ratio.
 98. $100 \times \frac{F_{\text{[O II]7330A}}}{F_{\text{H}\beta}}$ ratio error.
 99. $100 \times \frac{F_{\text{[Ar III]7751A}}}{F_{\text{H}\beta}}$ ratio.
 100. $100 \times \frac{F_{\text{[Ar III]7751A}}}{F_{\text{H}\beta}}$ ratio error.
 101. $100 \times \frac{F_{\text{[O II]8446A}}}{F_{\text{H}\beta}}$ ratio.
 102. $100 \times \frac{F_{\text{[O II]8446A}}}{F_{\text{H}\beta}}$ ratio error.
 103. $100 \times \frac{F_{\text{[S III]9069A}}}{F_{\text{H}\beta}}$ ratio.
 104. $100 \times \frac{F_{\text{[S III]9069A}}}{F_{\text{H}\beta}}$ ratio error.

This paper has been typeset from a $\text{\TeX}/\text{\LaTeX}$ file prepared by the author.